Impacts of tidally driven internal mixing in the Early Eocene Ocean

Jean-Baptiste Ladant[1], Jeanne Millot-Weil[1,*], Casimir de Lavergne[2], J. A. Mattias Green[3], Sébastien Nguyen[1], Yannick Donnadieu[4]

[1]Laboratoire des Sciences du Climat et de l'Environnement, LSCE/IPSL, CEA-CNRS-UVSQ, Université Paris-Saclay, 91191, Gif-sur-Yvette, France.

[2]Laboratoire d'Océanographie et du Climat : Expérimentations et Approches Numériques, IPSL, Sorbonne Université/IRD/CNRS/MNHN, Paris, France.

[3]School of Ocean Sciences, Bangor University, Menai Bridge, UK.

[4]Aix Marseille Université, CNRS, IRD, INRA, Coll France, CEREGE, Aix-en-Provence, France

Corresponding author: Jean-Baptiste Ladant (jean-baptiste.ladant@lsce.ipsl.fr)

[*]Now at: School of Geographical Sciences, University of Bristol, Bristol, UK.

Key Points:

- Inclusion of realistic near-field tidal mixing substantially modifies global deep ocean circulation in the Early Eocene.
- These tidally-driven changes yield significantly different biogeochemical properties of water masses, in particular in the Atlantic.
- The simulation that includes tidal mixing compares more favorably to inferences from the O_2 proxy record.

Abstract

Diapycnal mixing in the ocean interior is largely fueled by internal tides. Mixing schemes that represent the breaking of internal tides are now routinely included in ocean and earth system models applied to the modern and future. However, this is more rarely the case in climate simulations of deep-time intervals of the Earth, for which estimates of the energy dissipated by the tides are not always available. Here, we present and analyze two IPSL-CM5A2 earth system model simulations of the Early Eocene made under the framework of DeepMIP. One simulation includes mixing by locally dissipating internal tides, while the other does not. We show how the inclusion of tidal mixing alters the shape of the deep ocean circulation, and thereby of large-scale biogeochemical patterns, in particular dioxygen distributions. In our simulations, the absence of tidal mixing leads to a deep North Atlantic basin mostly disconnected from the global ocean circulation, which promotes the development of a basin-scale pool of oxygen-deficient waters, at the limit of complete anoxia. The absence of large-scale anoxic records in the deep ocean posterior to the Cretaceous anoxic events suggests that such an ocean state most likely did not occur at any time across the Paleogene. This highlights how crucial it is for climate models applied to the deep-time to integrate the spatial variability of tidally-driven mixing as well as the potential of using biogeochemical models to exclude aberrant dynamical model states for which direct proxies do not exist.

1. Introduction

Tides are the main supplier of diapycnal mixing in the ocean's interior, beneath the surface boundary layers (e.g., Egbert and Ray, 2000; Vic et al., 2019; de Lavergne et al., 2020). Barotropic tidal currents flowing over sloping bottom topography generate internal waves at tidal frequency, called internal tides (Garrett and Kunze, 2007). The propagation, non-linear interaction, and ultimate breaking of internal tides into three-dimensional turbulence constitutes the primary contribution to diapycnal mixing (that is, mixing across isopycnals) and thus to water mass transformation in the deep ocean (de Lavergne et al., 2022; Melet et al., 2022). There are multiple pathways and processes leading to the dissipation of internal tide energy. Small-scale internal tides tend to dissipate close to their generation site, whereas large-scale internal tides dissipate more remotely, sometimes thousands of kilometers away from the generation site (Whalen et al., 2020).

The modern global overturning circulation is usually schematized as a two-loop system, consisting of an adiabatic upper cell fed by deep convection in the North Atlantic (the NADW) overlying a largely diabatic lower cell fed by Antarctic Bottom Water (AABW) formation in the Southern Ocean (Marshall and Speer, 2012; Talley, 2013; Melet et al., 2022). Diapycnal mixing plays an important role in shaping this two-cell overturning circulation (Cimoli et al., 2023); in particular the tidally-driven, bottom-intensified, part of the mixing is instrumental in reducing the density of northward-flowing AABW and in mixing AABW with NADW (de Lavergne et al., 2022; Melet et al., 2022). It is the specific geometry of the modern Southern Ocean, with its continent-free latitudinal band down to a depth of ~ 2000 m at the Drake Passage, that favors the adiabatic upwelling of deep waters (NADW and Pacific/Indian Deep Waters) in the surface Ekman divergence of the Southern Ocean (Toggweiler and Samuels, 1995, 1998). This prompts the possibility that, in periods of the deep-time past of the Earth when the Drake and/or Tasman gateways were closed or shallow, diapycnal (diabatic) mixing may have played a greater role in setting the mode and intensity of the global overturning circulation (Green and Huber, 2013).

Since the seminal work of Munk (1966), great efforts have been made to understand what controls diapycnal mixing in the ocean interior (e.g., Munk and Wunsch, 1998; St. Laurent and Garrett, 2002; MacKinnon et al., 2017) and to refine the parameterizations of vertical diffusivity in ocean general circulation models (GCM) (e.g., Bryan and Lewis, 1979; Gargett, 1984; Simmons et al., 2004; Saenko and Merryfield, 2005; Jayne, 2009; Schmittner and Egbert, 2014; Melet et al., 2016; de Lavergne et al., 2020; Song et al., 2023). Recent work has comprehensively reviewed what is currently known about the role of ocean mixing in the climate system (Whalen et al., 2020; de Lavergne et al., 2022; Melet et al., 2022) and, in particular, the contribution of different internal wave processes (e.g., near-field and far-field internal tide dissipation, lee wave dissipation and wind-induced near-inertial wave energy dissipation) to the total mixing. The parameterization of all of these processes into global ocean models is a currently active area of research (MacKinnon et al., 2017) and, in climate models applied to the deep-time past of the Earth, such processes are generally ignored. Instead, mixing in the ocean interior is parameterized either by a constant background diffusivity coefficient or by simple schemes such as a horizontally uniform but depth varying diffusivity (Bryan and Lewis, 1979, hereafter BL).

In recent years though, some models applied to paleoclimate studies have started to include to contribution of local (near-field) internal tide dissipation (e.g., Schmittner et al., 2015; Hutchinson et al., 2018; Wilmes et al., 2021), following the bottom-intensified mixing parameterization of Simmons et al. (2004, hereafter S04). Wilmes et al. (2021) notably show that using appropriate Last Glacial Maximum tidal dissipation, instead of modern dissipation with otherwise glacial forcings, invigorates the circulation in the ocean interior and increases the fit with carbon isotope measurements. Hutchinson et al. (2018) compare the S04 scheme with the previously-implemented BL scheme in Late Eocene GFDL CM2.1 earth system model simulations and essentially find very little differences in terms of ocean circulation structure and intensity and of water mass age. This is somehow contradictory to the same exercise performed by Jayne (2009) using modern simulations carried out with the NCAR POP 1.4.3 ocean model. In the latter work, the change from the BL parameterization to an explicit tidal mixing scheme leads to small impacts on the simulated ocean heat transport (OHT) and upper ocean circulation (because of similar vertical diffusivity values there) but significantly increases the intensity of the deep circulation (Jayne, 2009).

Another approach has consisted in adding an explicit tidal contribution to the momentum equations rather than to the parameterization of vertical diffusivity (Weber and Thomas, 2017). Though limited to relatively short integration time (100 years in their 3° x 2° Early Eocene ECHAM5/MPIOM configuration) because the explicit tidal forcing requires high resolution simulations (Song et al., 2023), the simulations of Weber and Thomas (2017) report a weak impact of tidal forcing on OHT and large-scale ocean circulation shape but a more significant impact on the intensity of the overturning circulation, echoing the results of Jayne (2009).

More recently, Zhang et al. (2022) have explored the variability in ocean circulation in models participating to the DeepMIP project on the Early Eocene (Lunt et al., 2017), in which the models were forced by a set of Early Eocene forcings, identical across the models but for the details of their implementation. The authors report large inter-model differences in simulated ocean circulation structure and intensity (Zhang et al., 2022, their Figure 2). Interestingly, the model simulating the most intense overturning circulation (IPSL-CM5A2) is one of the only two DeepMIP models explicitly including a tidal-mixing contribution to vertical diffusivity.

Here, we investigate the impacts of the inclusion of near-field bottom-intensified tidal mixing (using the S04 parameterization) on the ocean circulation and biogeochemistry in the Early

Eocene. We demonstrate that failing to include abyssal turbulent mixing leads to a stagnant ocean with large areas of anoxia, which does not match proxy data from the Equatorial and North Atlantic.

2. Model and simulations

2.1. IPSL-CM5A2 Earth System Model

The simulations presented in this work are performed with the IPSL-CM5A2 Earth System Model (Sepulchre et al., 2020), itself composed of LMDZ for the atmosphere (Hourdin et al., 2013), ORCHIDEE for the land surface and vegetation (Krinner et al., 2005), and NEMO version 3.6 for the ocean (Madec and the NEMO team, 2016). NEMOv3.6 consists of the OPA dynamic ocean model, the LIM2 sea-ice model (Fichefet and Maqueda, 1997) and the PISCES-v2 marine biogeochemistry model (Aumont et al., 2015). OASIS (Valcke, 2013) is used to couple the models, and XIOS (Meurdesoif et al., 2016) handles input/output processing. LMDZ and ORCHIDEE shares the same horizontal resolution of 3.75° x 1.875° (longitude x latitude) and LMDZ is discretized into 39 uneven levels in the vertical. NEMO has a nominal horizontal resolution of 2°, enhanced to 0.5° at the equator, and 31 vertical levels whose thickness varies from 10 m at the surface to 500 m at the bottom. NEMO uses a tripolar grid to overcome the North Pole singularity (Madec and Imbard, 1996). Previous deep-time paleoclimate modeling with the IPSL-CM5A2 model (e.g., Laugié et al., 2021), including the IPSL-CM5A2 simulations carried out as part of the DeepMIP project (Zhang et al., 2020, 2022), used an oceanic domain extending down to 78°S. Here the numerical ocean grid has been regenerated and extended southward in latitude down to 85°S in order to better represent possible marine incursions at latitudes poleward of 78°S in intervals of the last 100 Ma. We note, however, that this represents a negligible issue in the standard DeepMIP paleogeography based on a hotspot reference frame that we use here, though this would not be the case in Early Eocene paleogeographies constructed with a paleomagnetic reference frame (Lunt et al., 2017).

2.2 Mixing in the ocean model

In this version of NEMO, vertical mixing in the water column is implemented as a Turbulent Kinetic Energy (TKE) closure model (Gaspar et al., 1990; Blanke and Delecluse, 1993). This

closure is complemented with a parameterization for convection, consisting of enhanced vertical diffusion where stratification is unstable (Lazar et al., 1999), a parameterization for double diffusive mixing (Merryfield et al., 1999), and a tidal mixing parameterization following S04. The vertical eddy diffusivity coefficient K_v is thus expressed as:

$$K_v = \max(K_0, K_{TKE}) + K_{ddm} + K_{Tides} \text{ for } N^2 > 0 \text{ (stable stratification)}$$
$$K_v = K_{EVD} \text{ otherwise}$$

with N the Brunt-Väisälä frequency, K_0 a background diffusivity effectively setting the minimum vertical diffusivity, K_{TKE} the diffusivity computed from the TKE scheme, K_{ddm} the diffusivity attributed to double diffusion, K_{Tides} the tidal diffusivity and K_{EVD} a prescribed constant convective diffusivity. Rigorously, the tidal and double diffusion schemes contribute to K_v even in regions of unstable stratification but the very large diffusivity value parameterizing convective processes renders these contributions negligible. Here, K_0 is set to 1.2 10^{-5} m^2 s^{-1}, K_{EVD} = 100 m^2 s^{-1} and K_{Tides} has the form:

$$K_{Tides} = \frac{q\Gamma EF}{\rho N^2} \qquad \text{(Eq. 1)}$$

where q is the tidal dissipation efficiency, Γ is the mixing efficiency, E is the tidal energy flux from Green and Huber (2013), ρ is the water density, N is the buoyancy frequency along the seafloor and F is a vertical structure function that decays exponentially with height above bottom:

$$F(z) = \frac{e^{-\frac{H+z}{h_0}}}{h_0\left(1-e^{-\frac{H}{h_0}}\right)} \qquad \text{(Eq. 2)}$$

with H the total depth of the water column and h_0 the vertical decay scale for turbulence. We use the standard model values of q = $\frac{1}{3}$, Γ = 0.2 and h_0 = 500 m (Madec and the NEMO team, 2016), which are identical to those originally chosen by S04.

2.3 PISCES Marine Biogeochemistry Model

The PISCES model (Pelagic Interactions Scheme for Carbon and Ecosystem Studies, Aumont et al., 2015) simulates the lower trophic levels of marine ecosystems (nanophytoplankton, diatoms, microzooplankton and mesozooplankton), carbonate chemistry and the biogeochemical cycles of carbon, oxygen, and the main nutrients (phosphorus, nitrogen, iron and silica). Dissolved oxygen is produced in the ocean by phytoplankton net primary production and consumed by zooplankton heterotrophic respiration, oxic remineralization of organic matter and nitrification. At the air-sea interface, dissolved oxygen is exchanged using the parameterization of Wanninkhof (1992). The atmospheric concentration of dioxygen is set to a fixed ratio of 0.21.

In the water column, PISCES explicitly represents two pools of organic matter particles that differ in their average size (i.e., large and small particles) and respective sinking speed, as well as a pool of semi-labile dissolved organic matter. The particle pools are degraded into the dissolved one as a function of temperature and oxygen concentrations. Dissolved organic matter undergoes oxic remineralization or denitrification depending on local oxygen levels. The remineralization and denitrification rates are function of temperature, oxygen and nitrate concentrations, and of the bacterial activity and biomass (Aumont et al., 2015). When reaching the ocean floor in the form of particles, organic matter is permanently buried or degraded by sedimentary denitrification or oxic remineralization. The proportion of buried carbon is dependent on the organic carbon flux at the bottom and is computed according to Dunne et al. (2007). The fraction of sedimentary denitrification versus oxic remineralization is computed using the meta-model of Middelburg et al. (1996). Degraded organic carbon is then released into the ocean bottom level in the form of DIC. Ocean bottom concentrations of dissolved oxygen and nitrate are also consumed to account for sedimentary oxic remineralization and denitrification, respectively (Aumont et al., 2015). In the absence of an explicit sediment module, the global inventories in phosphate, nitrate, silicate and alkalinity are restored to modern values so that the global mean ocean concentrations in these elements do not drift away from modern mean concentrations (Aumont et al., 2015). We also use an additional inert artificial tracer representing the age of water masses. This age tracer value is restored to 0 in the top 10 m of the model ocean and increases at a rate of one year per year deeper than 10 m (Bopp et al., 2017).

2.4 Experimental design

We present two numerical simulations of the Early Eocene based on the DeepMIP protocol (Lunt et al., 2017). The boundary and initial conditions are essentially those of the 840 ppmv simulations of Zhang et al. (2020), that is, we use the paleogeography of Herold et al. (2014) with a prescribed atmospheric CO_2 concentration of 840 ppmv. The orbital parameters of the Earth are those of present-day and other greenhouse gas concentrations are set to their preindustrial values. The simulations are therefore representative of a pre-Paleocene-Eocene Thermal Maximum interval, following the terminology of Lunt et al. (2017). The simulations are initialized with ocean temperature and salinity distributions as in Zhang et al. (2020) and only differ by the absence ("EE-noM2") or presence ("EE-std") of the contribution of near-field internal tide energy dissipation (K_{Tides}) to the vertical diffusivity coefficient. In the following, we will refer to the absence or presence of tidal mixing, though this is somewhat a misnomer because the contribution of background diffusivity (i.e. K_0) to vertical diffusivity is included in the two simulations. As described in S04, this background diffusivity may account for the far-field dissipation of large-scale internal tides as well as other sources of mixing that are not explicitly modeled, such as lee waves or wind-induced radiating near-inertial waves (e.g., Melet et al., 2022).

In NEMOv3.6, the tidal energy flux E includes components for the M2, K1 and S2 tides whereas Green and Huber (2013) provides an estimate only for the M2 tide (see Fig. S1 for a map of the estimated M2 dissipation). Considering that 1) the M2 component dominates the tide, and 2) the S2 energy flux is simply taken to be $\frac{1}{4}$ of the M2 energy flux in the NEMOv3.6 mixing scheme, we argue that using $\frac{5}{4}$ of the M2 estimate of Green and Huber (2013) as forcing in the model (M2 + S2 contributions) is a reasonable first step, despite the missing K1 contribution.

The two simulations are run for 5100 model years after which both have reached quasi-equilibrium with small residual trends in mean deep ocean (2750 – 4250 m) temperatures < 0.02°C/century (Fig. S2). The last 100 years of each model run are used to build a climatological average for the ocean dynamics. In order to improve the equilibration of biogeochemistry, we extend the simulations in an offline PISCES configuration for another 4000 model years. In this setup, the monthly-mean climatological ocean dynamics is repeatedly read by PISCES to calculate the evolution of the biogeochemical tracer fields. Again, we use the last 100 model years to build a climatological average for the ocean biogeochemistry.

3. Results

3.1 Energetic considerations

3.1.1 Available energy

The tidal model used by Green and Huber (2013) yields an estimate of 1.44 TW of energy dissipated in the Eocene ocean by the M2 barotropic tide, which, interpolated on the NEMO grid, amounts to 1.473 TW. Because the tidal mixing scheme in NEMO includes the S2 tidal contribution expressed as one-fourth of the M2 contribution, the total energy input from tides is 1.841 TW, of which only one-third, 0.614 TW, is assumed to dissipate locally and employed in the tidal mixing scheme (because q = $\frac{1}{3}$ in Equation (1) above).

The implementation of the tidal mixing scheme in the model is not fully consistent energetically for two reasons. First, a fraction of the energy input is lost in the lower half of the bottom cells, where stratification and diffusivity are not defined because of the no-flux boundary condition at the bottom. Second, the model parameterization imposes an upper bound of 3×10^{-2} $m^2.s^{-1}$ on the tidal diffusivity (Madec and the NEMO team, 2016). Diagnosing the energy effectively used by the tidal mixing scheme gives 0.42 TW, that is, about 70 % of the expected power (0.614 TW).

We can compute the power consumption due to vertical mixing processes, expressed as in S04:

$$P = \frac{1}{\Gamma} \int \rho K N^2 dV \qquad \text{(Eq. 3)}$$

Table 1 shows the amount of power consumed at the global scale and in each basin (Atlantic, Pacific, Indian, Tethys and Arctic, represented on Fig. S3). At the global scale, the total power consumed by diapycnal mixing in the model is 1.45 TW in EE-std. This is weaker than the 1.84 TW of total M2 + S2 tidal dissipation estimated by the model of Green and Huber (2013). Two considerations shed light on this difference. First, the effective consumption by tidal vertical mixing is only about 70 % of what is expected from Equation (1). Second, the background

diffusivity is simply prescribed and does not depend on the tidal dissipation; hence power consumption by background mixing cannot be expected to match the unused two-thirds of barotropic tidal energy loss.

Overall, we calculate that tidal mixing represents about 29 % of the total power consumed by diapycnal mixing in the ocean interior. This ratio is only slightly lower to that simulated by S04, somewhat surprisingly given the very different paleogeography and stratification of our simulations. At the basin scale and excluding the Arctic basin, the contribution from tides varies from 14 % of the total power in the Tethys basin to 32 % in the Pacific basin. This is consistent with larger mean dissipation rates in the Pacific and Indian Oceans than in the Atlantic and Tethys Oceans (Fig. S1).

3.1.2 Diapycnal diffusivity

The inclusion of tidal mixing substantially changes the amount of energy available to mix the deep ocean. Diapycnal diffusivities are therefore considerably different both horizontally and vertically in EE-std compared to EE-noM2.

In EE-noM2, the zonally averaged vertical diffusivity is generally close to the background value except in the surface mixed-layer depth, in which mixing due to the winds generates elevated vertical diffusivity, and in the Southern Ocean where deep convection processes mix waters down to the abyss (Fig. 1a, c, e). At mid depths (2000 – 3000 m), the zonal mean vertical diffusivity is elevated throughout the low latitudes (Fig. 1a). This signal mostly originates from a relatively isolated abyssal sub-basin in the eastern Pacific Ocean between the East Pacific Rise and the American continent (Fig. 1e) in which the weak stratification elevates K_{TKE} and stimulates episodic convective instabilities. At 600 m depth (Fig. 1c), away from turbulent wind-driven mixing, vertical diffusivity is close to the background value K_0 except in deep convection zones of the Southern Ocean. Because the 600 m geopotential surface is also generally far from bottom topography, adding tidal mixing in EE-std does not significantly alter vertical diffusivity at this depth (Fig. 1d), except in deep-water formation zones close to the Antarctic margins. By contrast, diffusivity at 3000 m depth is enhanced by about 2 orders of magnitude in broad regions of the Pacific and Indian Oceans in EE-std relative to EE-noM2 (Fig. 1f). Note that because tidal mixing is implemented here as a bottom-intensified energy dissipation, and because stratification generally decreases with depth, the maximum tidal diffusivity in the vertical is found locally on the deepest ocean grid cell. The Atlantic basin in

the Eocene configuration exhibits a weaker tide than the Pacific (Green and Huber, 2013, see also Fig. S1) and, therefore, vertical diffusivity does not increase as much as in the Pacific Ocean in EE-std compared to EE-noM2. The zonally averaged vertical diffusivity essentially shows that diapycnal mixing is substantially enhanced in the ocean interior. As we will show in the next sections, the additional mixing energy available in the deep ocean has profound consequences on the intensity of the overturning circulation and the pathways of water masses.

3.2 Surface changes

The upper-ocean (0 – 100 m) annual mean temperatures in EE-noM2 are roughly close to 10°C in the Southern Ocean and to 5°C in the quasi-enclosed Arctic Ocean (Fig. 2a). They increase equatorward to reach up to more than 37°C in the equatorial western Pacific. As expected from similar simulations performed with the same model, this temperature distribution is really close to that presented on Figure 2a of Zhang et al. (2020) (see Fig. S4 for a more detailed comparison). Tidally-driven mixing leads to large changes in the Southern Ocean surface layer. The Atlantic and Indian sectors of the Southern Ocean are warmer (locally more than 4K) in EE-std than in EE-noM2 (Fig. 2b), whereas the Pacific sector is cooler, although the change is smaller. Warmer (cooler) regions of the Southern Ocean in EE-std are also regions of increased (decreased) upper ocean salinity (not shown).

In EE-noM2, deep convective areas are exclusively found in the Southern Ocean, in the Atlantic, Indian and Pacific sectors (Fig. 2c), and there is no deep-water formation in the Northern Hemisphere. The upper-ocean temperature changes in EE-std are sustained by increased deep-water formation in the Atlantic and Indian sector of the Southern Ocean compared to EE-noM2 as can be seen by the deepening of the winter mixed layer depth (MLD) in these areas (Fig. 2d). In the South Atlantic, the MLD deepens by more than 1000 m and enhances the temperature and salt advection feedback from the lower latitudes. In the Pacific sector, the winter MLD instead slightly decreases, driving the opposite change in the advection feedback. Figure S5 further shows that the deepening/shoaling of MLD in EE-std relative to EE-noM2 is robust across the simulations and not simply an artifact of the averaging period.

3.3 Ocean circulation changes

The increase in available energy for mixing is reflected by a significant enhancement of the global meridional overturning circulation (MOC) (Fig. 3). The MOC in the two simulations has a roughly comparable shape consisting of a single anticlockwise overturning cell in the Southern Hemisphere fed by deep-water formation in the Southern Ocean. The intensity of the MOC and the penetration of deep-water in the abyss is however greater in EE-std than in EE-noM2, although the maximum rate of overturning is similar in the two simulations (~ 35 Sv at 2000 m depth in EE-std and at 900 m depth in EE-noM2). Away from the Southern Ocean, the additional tidal mixing energy sustains a stronger and deeper overturning cell extending up the northern mid to high latitudes (8 Sv at 2000 m depth and 30°N in EE-std, Fig. 3b), effectively increasing the ventilation of the EE-std ocean compared to EE-noM2 and acting to reduce vertical tracer gradients.

This homogenization is evident from the global zonal mean distribution of temperature (Fig. S6), which shows a globally warmer deep ocean (below ~ 1000 m) and a globally cooler upper and intermediate ocean in EE-std compared to EE-noM2 at all latitudes except those of the Southern Ocean (80°S – 40°S) where the ocean is globally warmer throughout the water column. The EE-std ocean is thus more vertically well mixed than the EE-noM2 ocean.

The intensification of the global MOC has interesting consequences on the water mass pathways, in particular in the Atlantic. Figure 4 shows the ocean current velocity and direction at different depths in the South Atlantic and Southern Ocean. At 500 m depth, the western boundary current flowing southward off the coast of South America is substantially increased in EE-std. This increase confines the westward-flowing water masses close to Antarctica to the Southern Ocean, whereas in EE-noM2, these waters mix with those from the South Atlantic western boundary current towards the Indian Ocean. Deeper in the water column (1400 - 1800 m depth), the water masses flowing from the Atlantic to the Indian sector of the Southern Ocean in EE-noM2 consist of recirculated waters from the Southern Ocean and locally-formed deep waters, as the southward-flowing Atlantic western boundary current is absent. In contrast, in EE-std, the southward western-boundary current is still active and contributes to exporting water masses from the low-latitude Atlantic toward the Indian Ocean. In the abyss (3250 – 3750 m), only a very small fraction of the Southern Ocean water masses flows northward in the Atlantic in EE-noM2 while most are exported eastward to the Indian Ocean. In EE-std an intense northward current advects water masses along the western side of the basin into the Equatorial and North Atlantic.

These results demonstrate that the deep Equatorial and North Atlantic Oceans are more isolated from the global ocean circulation below ~ 1500 m in EE-noM2 than in EE-std. In the Early Eocene, the deepest connections of the Atlantic basin are with the Southern Ocean because the Central American, Tethys (Gibraltar) and Atlantic-Arctic gateways are all shallow and/or narrow. Since the bathymetric configuration does not change between the two simulations, the increased isolation of the EE-noM2 Equatorial and North Atlantic Oceans is purely caused by lower levels of deep turbulent mixing, leading to major differences in Atlantic stratification and circulation. In EE-std, tidal mixing renders abyssal water masses increasingly more buoyant as they flow away from deep-water formation areas in the Southern Ocean whereas the buoyancy gain across the Atlantic is weaker in EE-noM2. The isopycnal located at approximately 3000 m depth at 45°S (the 40.08 and 39.98 $kg.m^{-3}$ σ_3 contour in EE-noM2 and EE-std respectively, Fig. 5) indeed deepens to about 3400 m depth in EE-noM2 and 4500 m depth in EE-std at 35°N. In other words, isopycnals of similar depth in the deep South Atlantic exhibit depth difference in excess of 1 km upon reaching the deep North Atlantic. The larger northward deepening of the isopycnals across the deep Atlantic generates a stronger meridional pressure gradient and, thus, forces a more active deep northward circulation (e.g., Whitehead, 1998) in EE-std compared to EE-noM2, leaving the latter more stagnant.

3.4 Biogeochemical changes

The more active deep circulation with tidal mixing also yields a significant reorganization of the marine biogeochemistry in the deep ocean, in particular in the Atlantic. At the global scale, though it is once again more evident in the Atlantic (Fig. 5c and d), the deep ocean ventilation is reduced in the absence of tidal mixing. Notably, deep North Atlantic water masses are almost 3 times older in EE-noM2 than in EE-std. These deep water masses therefore exhibit very different biogeochemical properties in EE-noM2 and EE-std, and this is particularly visible on the distribution of dissolved oxygen across the water column.

In EE-noM2, the deep North Atlantic water masses possess the biogeochemical signature of very old water masses: rich in nutrients and dissolved inorganic carbon (DIC) and poor in oxygen. In fact, the North Atlantic is spectacularly oxygen-depleted (Fig. 6a), with hypoxia (defined here as the 62.5 $mmol.m^{-3}$ level) reached over the whole water column in the low latitudes of the North Atlantic (0 – 20°N) and below 800 m northward of 30°N. Anoxic levels

436 are reached northward of 20°N at depths between 1500 and 3000 m. The North Atlantic seafloor
437 is fully hypoxic and most of the coastal seafloor is anoxic (Fig. 6c). In contrast, deep North
438 Atlantic DIC and phosphate concentrations are high (Figs. S7 and S8) because falling organic
439 matter has been remineralized along the water mass journey and nutrients have therefore
440 accumulated in the deep ocean. Nitrate concentrations, however, rather decrease northward in
441 the deep Atlantic (Fig. S9) because the depletion in oxygen in this ocean basin triggers
442 denitrification to continue the remineralization process.
443
444 In EE-std, the younger water masses in the deep North Atlantic are relatively rich in oxygen
445 (Fig. 6b) and the seafloor is well oxygenated with only very limited hypoxic coastal areas. The
446 North Atlantic exhibits higher nitrate concentrations in EE-std than EE-noM2 in the deep (Fig.
447 S9), because the oxygen levels are above those required to trigger denitrification, and we find
448 lower DIC and phosphate concentrations (Figs. S7 and S8), as expected for better ventilated
449 water masses.
450
451 There are three main processes controlling the oxygenation of water masses in the ocean:
452 surface atmosphere-ocean interaction controlling the degree of solubility of O_2 in the ocean,
453 ocean circulation, and biological activity. Dissolved O_2 concentrations in the ocean can be
454 decomposed into a thermal and a non-thermal component, referred to as the saturation
455 component (O_{2sat}) and the Apparent Oxygen Utilization (AOU) respectively. O_{2sat} is the
456 concentration of O_2 that can be dissolved for a given temperature and salinity whereas AOU
457 integrates the contribution of ocean circulation and biology. These quantities are related as
458 such:
459 $$O_2 = O_{2sat} - AOU$$
460
461 As shown on Figure 7 for EE-noM2, surface O_{2sat} increases poleward because solubility
462 increases with decreasing temperatures (Fig. 7b). Surface O_2 concentrations are generally close
463 to O_{2sat} because, besides interacting with the atmosphere, the upper ocean layers gain dissolved
464 O_2 as the result of photosynthesis of marine phytoplankton. The AOU is therefore low (e.g., the
465 surface mid-latitudes on Fig. 7c). One notable exception is the equatorial subsurface ocean
466 because it is a region of upwelling that brings to the upper ocean water masses extremely rich
467 in nutrients allowing for intense phytoplanktonic activity. Consequently, large amounts of
468 organic matter sink and consume oxygen at a rate faster than the one at which the ocean restores
469 its O_2 concentration by atmospheric exchange.

In the intermediate and deep ocean, O_2 concentrations are close to O_{2sat} in the Southern Ocean where deep convection occurs (Fig. 7a and b). As water masses age in the ocean interior (Fig. 7d), O_2 concentrations depart from O_{2sat} because of the increasing influence of remineralization processes that consume oxygen in the water column (reflected by the increasing AOU, Fig. 7c). In the deep North Atlantic, extremely old water masses that have not been in contact with the atmosphere for more than a millennium exhibit AOU values almost equal to O_{2sat}, indicating that almost all the available O_2 has been consumed.

Any change in dissolved O_2 concentrations between EE-noM2 and EE-std can therefore be partitioned into the change in O_{2sat}, reflecting the change in temperature and, to a lesser extent, salinity between EE-std and EE-noM2 and the change in AOU, which reflects circulation and biological changes:

$$\Delta O_2 = \Delta O_{2sat} - \Delta AOU$$

In the Atlantic, the changes in dissolved O_2 concentrations are almost fully explained by changes in AOU (Fig. 8). Interestingly, Figure 8 shows that contours of ΔAOU and of the water age difference between EE-std and EE-noM2 are very well correlated, thereby strongly hinting that the primary driver of oxygen changes is the reorganization of the ocean circulation following the addition of tidally-driven mixing. This is also confirmed by the limited changes in export productivity to the intermediate and deep ocean (Fig. S10).

4. Discussion

Our simulations compellingly demonstrate the crucial role played by tidally-driven abyssal turbulent mixing in shaping the circulation and the distribution of biogeochemical tracers in the ocean interior. However, apart from a few sensitivity simulations (Thomas et al., 2014; Weber and Thomas, 2017; Hutchinson et al., 2018), most earth system models applied to deep-time climates generally neglect tidally-driven mixing as a specific forcing and alter (or not) spatially-constant coefficients in the implemented vertical mixing parameterization (e.g., Bryan and Lewis, 1979) as a workaround (e.g., Zhang et al., 2022).

503 Hutchinson et al. (2018) find weak differences in terms of MOC shape and intensity and water
504 mass age between the standard BL scheme used in their CM2.1 Late Eocene simulations and
505 the same S04 bottom intensified mixing scheme as used here, indicating that the simulated
506 ocean circulation is largely similar. This is somewhat contradictory to the large change in MOC
507 intensity (and water age) found in our simulations, and we suggest a couple of explanatory
508 avenues. First, the standard BL scheme in Hutchinson et al. (2018) makes diffusivity increase
509 with depth—although without spatial dependence—and, as such, it is not rigorously similar to
510 prescribing a uniform background diffusivity coefficient K_0. We note however that, comparing
511 the BL and S04 schemes in a modern configuration, Jayne (2009) observes a large enhancement
512 of the intensity of the deep cell of the MOC in S04 with little change in MOC structure, much
513 as we observe in our simulations. Second, though Hutchinson et al. (2018) apply the same S04
514 scheme as we do, their input dissipation rate E is recomputed directly using equation (2) of S04
515 and a uniform seafloor roughness amplitude whereas we prescribe E based on the explicit tidal
516 model of Green and Huber (2013). This results in quite different mean vertical diffusivities at
517 a basin-scale. In particular, their mean Atlantic diffusivity, when using the tidal scheme, is
518 much enhanced compared to their mean Pacific diffusivity, whereas we find the opposite ratio
519 in our simulations (Fig. S11 and Fig. 9 of Hutchinson et al., 2018). Our results are in agreement
520 with the enhanced Pacific dissipation found in the tidal model results of Green and Huber
521 (2013). Because the specifics of the calculation of the dissipation rate E are missing in
522 Hutchinson et al. (2018), it still remains unclear at this stage whether these differences stem
523 from (i) the spatial variability of the tidal forcing (which may be absent in Hutchinson et al.,
524 2018), (ii) a different model implementation of the S04 tidal dissipation scheme, (iii) the change
525 in tidal forcing across the 15 Myrs separating the Early and Late Eocene, or (iv) different levels
526 of spurious numerical mixing in GFDL-CM2.1 and IPSL-CM5A2 (e.g., Holmes et al., 2021).
527 This nonetheless suggests that the spatial distribution of the tidal forcing significantly alters the
528 simulated ocean circulation (Saenko, 2006; Jayne, 2009).
529
530 Using CCSM3-forced MITgcm simulations of the Early Eocene, which includes a Bryan-Lewis
531 diffusivity profile and an older reconstruction of the paleogeography, Thomas et al. (2014)
532 found that increasing the diffusivity beyond the standard BL coefficients allow for a large
533 increase in the intensity of the MOC and yield a circulation mode that compares better to
534 compiled Pacific ε_{Nd} data, in particular in the case in which abyssal mixing is increased. In an
535 additional sensitivity experiment, the authors increased the mixing approximately fivefold
536 throughout the water column; doing this significantly enhanced the poleward OHT and reduced

the meridional surface temperature gradients, in agreement with inferred proxy data as well as previous investigations of increased upper ocean mixing effect on OHT (e.g., Jayne, 2009). In our simulations, the meridional SST gradient is only weakly affected by the addition of tidal mixing because vertical diffusivity in the upper 1000 m is similar in EE-noM2 and EE-std (Fig. S11). Below 1000 m, diffusivity (and meridional transport) increases substantially in EE-std but the vertical temperature gradient does not (Fig. S6) and the change in heat transport is small. Thomas et al. (2014) however note that sustaining such elevated diffusivity across the water column would require more than 20 TW; an amount of energy that tides cannot account for (Green and Huber, 2013) and whose source has yet to be found.

Using the ECHAM5/MPIOM model with the Early Eocene paleogeography of Heinemann et al. (2009), Weber and Thomas (2017) also investigated the response of the Eocene ocean circulation to tides. They simulate the change in ocean circulation in a similar setup than the one presented here, although the inclusion of tides in their model is represented by an additional, explicit, tidal forcing on the momentum equations rather than the parameterization of the contribution of tides to vertical diffusivity (Song et al., 2023). The simulated ocean circulation of Weber and Thomas (2017) exhibits deep-water formation in the Southern Atlantic, as here, but also in the North Atlantic. As in our experiments, adding tidal influence does not substantially modify the location of deep-water formation regions, in contrast to the penetration depth of these deep waters, but the limited integration time of their tidal simulation (100 years) prompts the possibility that it might not have reached sufficient equilibrium. One possible reason, among others (see, e.g., Zhang et al., 2022), explaining the different regions of deep convective activity is the paleogeographic reconstruction, which, in Weber and Thomas (2017), possesses in particular closed Drake Passage and Tasman Gateway and a more widely opened Central American Seaway compared to the Herold et al. (2014) reconstruction that we use. We indeed note that the recent DeepMIP study of Zhang et al. (2022) on Early Eocene ocean circulation highlights that all of the models—with the Herold et al. (2014) paleogeography—produce deep-water formation in the Southern Ocean (regardless of the sector) at the exception of the GFDL model, which exhibits deep convective activity in the North Pacific, and the NorESM model, which does not exhibit any deep-water formation, possibly because of insufficient spinup. In contrast, the models do not produce deep-water formation in the North Atlantic. Though the details of the ocean circulation differ between our simulations and those of Weber and Thomas (2017), the addition of tidal mixing has similar effects on the simulated circulation. Weber and Thomas (2017) also report an increase in the intensity of the MOC but

hardly any increase in ocean heat transport, in keeping with the notion that the impacts of the Eocene tide are concentrated in the abyssal ocean (Green and Huber, 2013).

In a recent comparison of the S04 tidal mixing scheme vs. explicit tidal forcing, both approaches were implemented in the FESOM2 ocean model (Song et al., 2023).The authors conclude that while the parameterized tidal mixing may miss some potentially important effects, such as the enhancement of bottom drag and continental shelf viscous dissipation, the explicit tidal forcing typically requires resolution of the order of 0.1° to produce realistic impacts. As a result, lower resolution simulations compare less favorably to observed hydrography with this scheme than with the S04 parameterization. It also makes the inclusion of explicit tidal forcing currently inapplicable to long-term deep-time climate simulations (Song et al., 2023).

Other studies have attempted to simulate the biogeochemical state of the Early Eocene (e.g., Heinze and Ilyina, 2015), generally in order to focus on the PETM perturbation (Winguth et al., 2012; Meissner et al., 2014; Ilyina and Heinze, 2019). In particular, Winguth et al. (2012) and Heinze and Ilyina (2015) have used modelling setups consisting of biogeochemical models of resolution and complexity similar to PISCES and forced by or coupled to ocean-atmosphere general circulation models, but the prescribed paleogeography and atmospheric CO_2 bear no consistency between the studies unlike more recent coordinated efforts such as DeepMIP (Lunt et al., 2017, 2021). Deep O_2 concentrations exhibit large differences between the simulations: the 1120 ppmv CO_2 simulation of Winguth et al. (2012) generates a well oxygenated Pacific Ocean and a more poorly oxygenated Atlantic Ocean whereas the 560 ppmv CO_2 simulation of Heinze and Ilyina (2015) shows a better oxygenated Atlantic than Pacific Ocean. In our simulations with tidal mixing at 840 ppmv, the deep Atlantic is better oxygenated than the Pacific (Fig. S12) but the equatorial Atlantic oxygen minimum zone is more developed and has lower O_2 concentrations. Interestingly, the primary production patterns in the upper ocean are more similar, with for instance intense primary production in most of the equatorial Pacific, in the eastern side of the Pacific and Atlantic Oceans as well as in the Southern Ocean. This suggests that the diversity in O_2 distributions across the simulations largely reflects the simulated ocean circulation, at least in the deep ocean.

There is currently no quantitative proxy for O_2 concentrations in the past, although semi-quantitative multi-proxy approaches can provide estimates of poorly oxygenated bottom water conditions ($\leq$ 50 μmol/kg) (Lu et al., 2020). Most studies therefore report qualitative estimates

of the local oxygenation state of the ocean relative to a baseline value, using redox-sensitive proxies such as the I/Ca ratio (e.g., Zhou et al., 2014, 2016), trace elements like molybdenum or manganese (Dickson et al., 2012, 2014; Pälike et al., 2014) or magnetofossils (Xue et al., 2022, 2023). Anoxic bottom water masses are perhaps more easily identifiable because the sedimentary abundance of trace elements is strongly redox dependent and sedimentary enrichment above average crustal values via complexification with sulfide elements is interpreted as reflecting high dissolved sulfide concentrations and thus anoxic/euxinic conditions (Dickson et al., 2012, 2014). If the distribution of Early Eocene redox archives is relatively global (though concentrated in the peri-Tethys area, see Figure 6 of Carmichael et al., 2017), the information conveyed by these estimates remains potentially strongly influenced by local settings (Clarkson et al., 2021). A complementary approach therefore consists in estimating the global area or volume occupied by anoxic or euxinic waters, using the isotopic ratio of molybdenum (Dickson et al., 2012), sulfur (Yao et al., 2018) or uranium (Clarkson et al., 2021), rather than reporting local estimates of bottom water oxygenation. For instance, combining uranium isotope measurements from ODP Site 865 (Allison Guyot, equatorial Pacific Ocean), DSDP Site 401 (Bay of Biscay, northeast Atlantic Ocean) and ODP Site 690 (Maud Rise, Atlantic sector of Southern Ocean) with box modelling, Clarkson et al. (2021) propose a maximal extent of seafloor anoxia of 0.25 % prior to the PETM perturbation and 2 % at the PETM.

In the following, we compare the simulated oxygen concentrations in EE-noM2 and EE-std with available data across a transect in the Atlantic using reported oxygen conditions at each site (Fig. 9) and compute the extent of anoxic seafloor simulated by the model. Three main observations can be made. First, the qualitative nature of the proxy leaves room for various interpretations. At the exception of Site 1262 and 1266 at Walvis Ridge for whose oxygen-rich conditions have been reported by the different proxies (Pälike et al., 2014; Xue et al., 2022), low oxygen content is estimated at every site but the degree of oxygen deficiency is unclear because anywhere between the anoxic (0 µmol/L) and hypoxic threshold (~ 60 – 70 µmol/L, Lu et al., 2020; Laugié et al., 2021). Second, at face value, the simulated O_2 concentrations are probably too low in EE-noM2, in particular in the North Atlantic, and too high in EE-std. Third, the fact that reported qualitative oxygen conditions in the data on Figure 9 reflect pre-PETM conditions and that most of these proxies suggest decreasing oxygen concentrations across the PETM perturbation but without extensive anoxia leads to the conservative assumption that the pre-PETM ocean did not exhibit large-scale conditions too close to anoxia. In this regard, the

simulated oxygen concentrations suggest that the ocean biogeochemical state in EE-noM2 is probably aberrant. This is confirmed by our calculation of the extent of anoxic seafloor, respectively 2.3 % in EE-noM2 and 0.1 % in EE-std, which also suggests an excess in oxygen depletion in EE-noM2 compared to pre-PETM estimates (Clarkson et al., 2021).

In addition, here, we do not *stricto sensu* model the biogeochemical conditions of the pre-PETM as, for instance, the global mean nutrient concentrations in phosphate, nitrate, alkalinity and silicate in the ocean are identical to the modern. Recent statistical box-modelling instead suggests that the marine phosphate concentrations reached a peak in the Paleogene, thus promoting higher primary productivity and lower deep-ocean O_2 concentrations (Sharoni and Halevy, 2023). All else being equal, prescribing a higher marine nutrient content in our simulations would decrease oxygen concentrations in both EE-noM2 and EE-std but with opposite effect on the model-data comparison. In EE-std, this would reduce the model-data mismatch because simulated O_2 concentrations are likely too high whereas in EE-noM2, it would increase the proportion of anoxic waters and thereby increase the mismatch with estimates from the geological record. The model-data mismatch in EE-std could be even further reduced with a better representation of the smaller meridional temperature gradients that are inferred from proxy data (e.g., Huber and Caballero, 2011; Evans et al., 2018) because this would act to reduce the amount of oxygen stored in surface waters, and therefore decrease O_2 concentrations throughout the water column. This also implies that the simulated O_2 concentrations in EE-noM2 are likely a conservatively "high-concentration" estimate and thus that the aberrant biogeochemical state likely reflects an aberrant Early Eocene dynamical ocean in EE-noM2.

Finally, we note that the input energy dissipation from the M2 tide that was used here is not exactly appropriate because the tidal model of Green and Huber (2013) was run with the ocean stratification obtained from the low-resolution equilibrated CCSM3 simulations discussed in Liu et al. (2009) instead of having been run with the IPSL-CM5A2 stratification. However, these simulations use a bathymetry close to that used in Green and Huber (2013) and the abyssal tidal dissipation is relatively insensitive to moderate changes in stratification. In addition, both our simulations and those of Liu et al. (2009) exhibit deep-water formation in the Southern Ocean. We thus argue that our results would not be significantly affected if the stratification from our simulations had been used in the tidal model simulations. In contrast, a larger impact is likely to be expected by the use of a higher-resolution bathymetric dataset in an improved

version of the tidal inversion model of Green and Huber (2013), such as that proposed in Green et al. (2023), and we ambition to investigate this possibility in a near future. Alternatively, a promising way lies in the use of comprehensive tidal mixing schemes accounting for both near-field and far-field dissipation of internal tides (de Lavergne et al., 2020), rather than schemes fixing vertical diffusivity, such as the BL scheme, or including only near-field mixing, such as the S04 scheme used here.

Conclusion

Using Early Eocene IPSL-CM5A2 earth system model simulations, we demonstrate the critically-overlooked impact of including a realistic estimate of the abyssal mixing driven by the near-field dissipation of internal tides in deep-time paleoclimate simulations. In our simulations, the global deep ocean circulation is substantially altered by the inclusion of abyssal tidal mixing, in particular in the Atlantic basin, and the global meridional overturning circulation is more intense and penetrates deeper in the ocean interior. This consequently drives large changes in the biogeochemical properties of deep water masses. In particular, we show that failing to include this abyssal turbulent mixing leads to a stagnant deep North Atlantic ocean with large anoxic areas that compares less favorably to qualitative reconstruction of paleo-oxygenation for this period than the more vigorous deep Atlantic ocean simulated in the experiment with realistic tidal mixing. Our results therefore stress the importance of routinely including abyssal turbulent mixing in upcoming deep-time paleoclimate studies and underline how the use of an adjunct biogeochemical model can help disentangle dynamical ocean modes for which proxies are lacking.

Acknowledgment

This work used computing hours on the HPC resources of the TGCC under GENCI allocations A0110102212 and A0130102212. We are grateful to Olivier Marti, Laurent Bopp, Olivier Aumont and Christian Ethé for discussions and help with the simulation setup. NCL (https://www.ncl.ucar.edu) was used to make figures and most analyses, in addition to Fortran. Figures use color maps developed by Fabio Crameri (Crameri et al., 2020). JAMG acknowledges funding from the UK Natural Environment Research Council (grants NE/F014821/1 and NE/S009566/1). YD acknowledges funding from the National Agency for

Research (ANR) project OXYMORE (grant 18-CE31-0020). The authors declare no conflict of interest.

Data availability

Code availability. LMDZ, NEMO (including PISCES), ORCHIDEE and XIOS are released under the terms of the CeCILL license. OASIS-MCT is released under the terms of the Lesser GNU General Public License (LGPL). IPSL-CM5A2 source code is available via modipsl with the command lines:

svn co -r 6039 https://forge.ipsl.jussieu.fr/igcmg/svn/modipsl/trunk modipsl;

cd modipsl/util; ./model IPSLCM5A2.2

The model revision numbers used in this work can be found in the modipsl/util/mod.def file:

- NEMOGCM branch nemo_v3_6_STABLE revision 6665
- XIOS2 branchs/xios-2.5 revision 1903
- IOIPSL/src svn tags/v2_2_2
- LMDZ5 branches/IPSLCM5A2.1 rev 3907
- ORCHIDEE branches/ORCHIDEE-IPSLCM5A2.1 rev 7376
- OASIS3-MCT 2.0_branch (rev 4775 IPSL server)

We recommend to refer to the project website for a proper installation and compilation of the environment:

https://forge.ipsl.jussieu.fr/igcmg_doc/wiki/Doc/Config/IPSLCM5A2, last access: 21/11/2023.

Model outputs. NetCDF outputs and scripts to produce the figures used in this study are stored at https://doi.org/10.5281/zenodo.10246071.

Tables and figures

		Power consumption used for diapycnal mixing (TW)			Fraction of power consumption due to tides
		K_0	Tides	Total	
Global	EE-std	1.03	0.422	1.45	0.29
	EE-noM2	1.02	0	1.02	0
Pacific	EE-std	0.590	0.282	0.872	0.32
	EE-noM2	0.584	0	0.584	0
Atlantic	EE-std	0.162	0.0560	0.218	0.26
	EE-noM2	0.160	0	0.160	0
Indian	EE-std	0.145	0.0661	0.211	0.31
	EE-noM2	0.140	0	0.140	0
Tethys	EE-std	0.109	0.0175	0.127	0.14
	EE-noM2	0.108	0	0.108	0
Arctic	EE-std	0.0278	$5\ 10^{-4}$	0.0283	0.02
	EE-noM2	0.0255	0	0.0255	0

Table 1. Power consumed by diapycnal mixing and fraction of power consumption due to tides calculated at the global-scale and for individual basins shown on Figure S3.

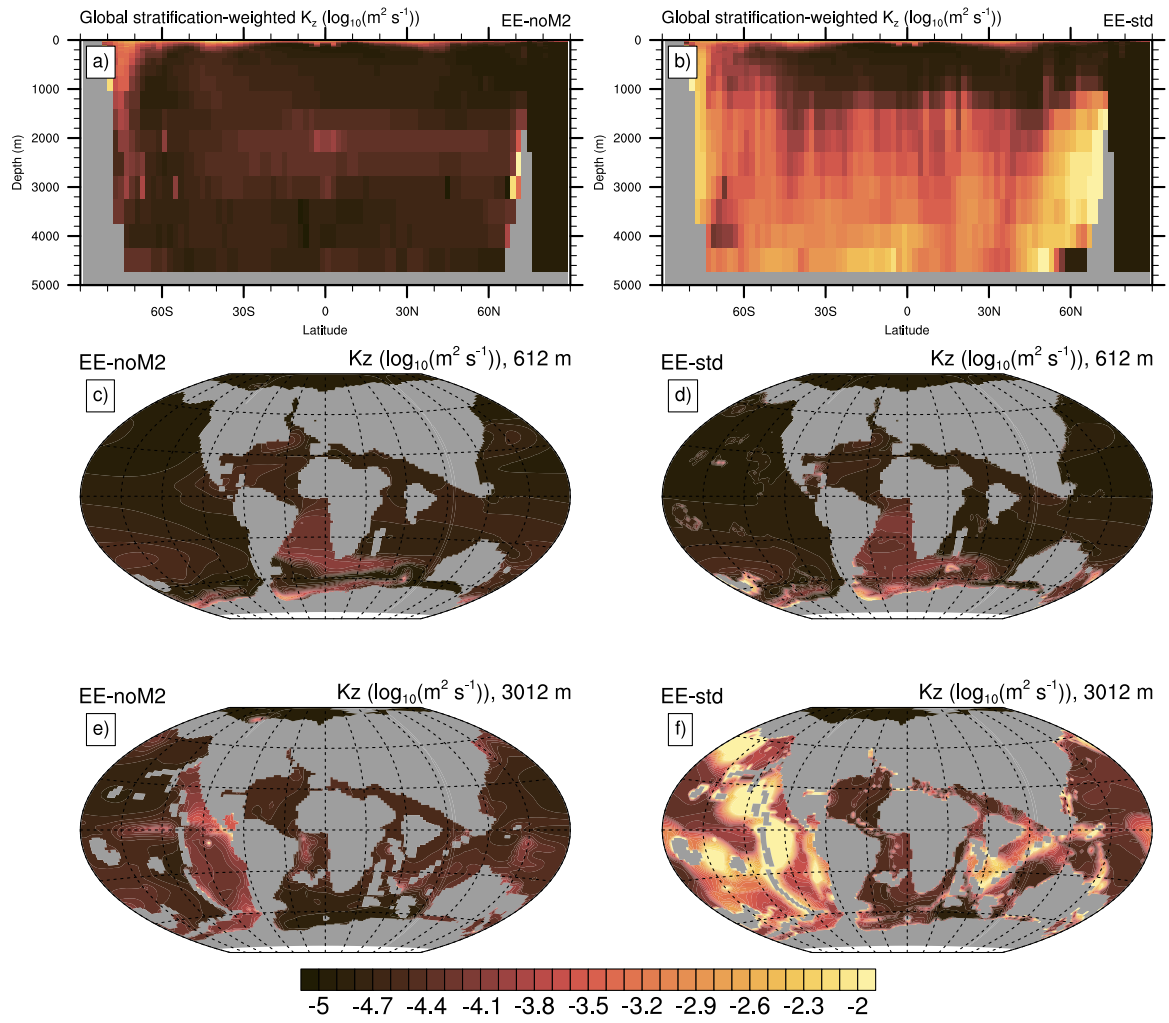

Figure 1. Stratification-weighted global zonal average of vertical diffusivity for EE-noM2 (a) and EE-std (b) ($\log_{10}(m^2\ s^{-1})$. Diffusivity at 600 m and 3000 m for EE-noM2 (c, e) and EE-std (d, f) ($\log_{10}(m^2\ s^{-1})$.

745

746

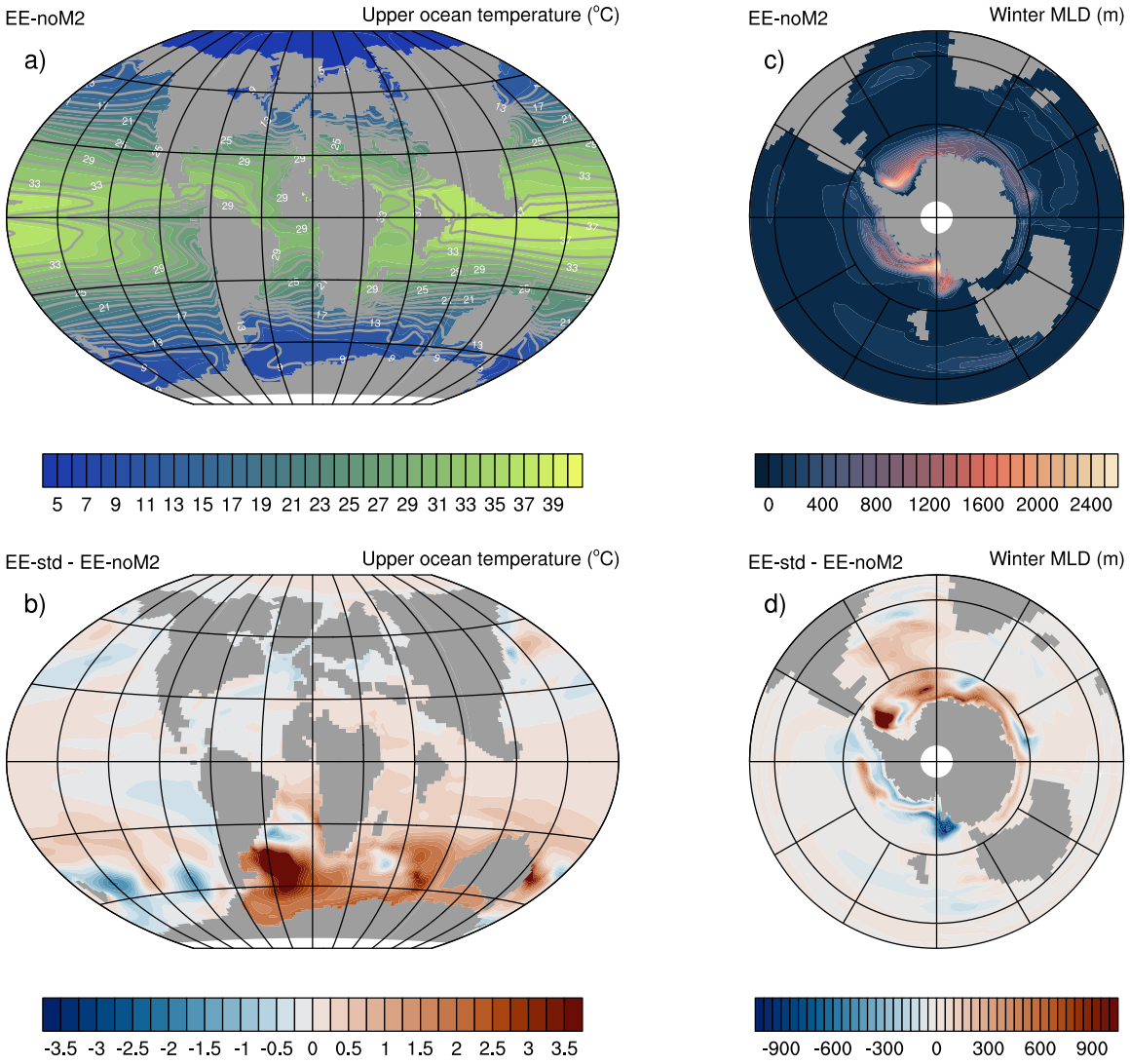

Figure 2. (a) EE-std mean annual upper ocean (0-100 m) temperatures (°C). (b) Mean annual upper ocean temperature (0-100 m) difference (°C) between EE-noM2 and EE-std. (c) Mean winter MLD (m) in EE-noM2. (d) Mean winter MLD difference (m) between EE-std and EE-noM2.

747

748

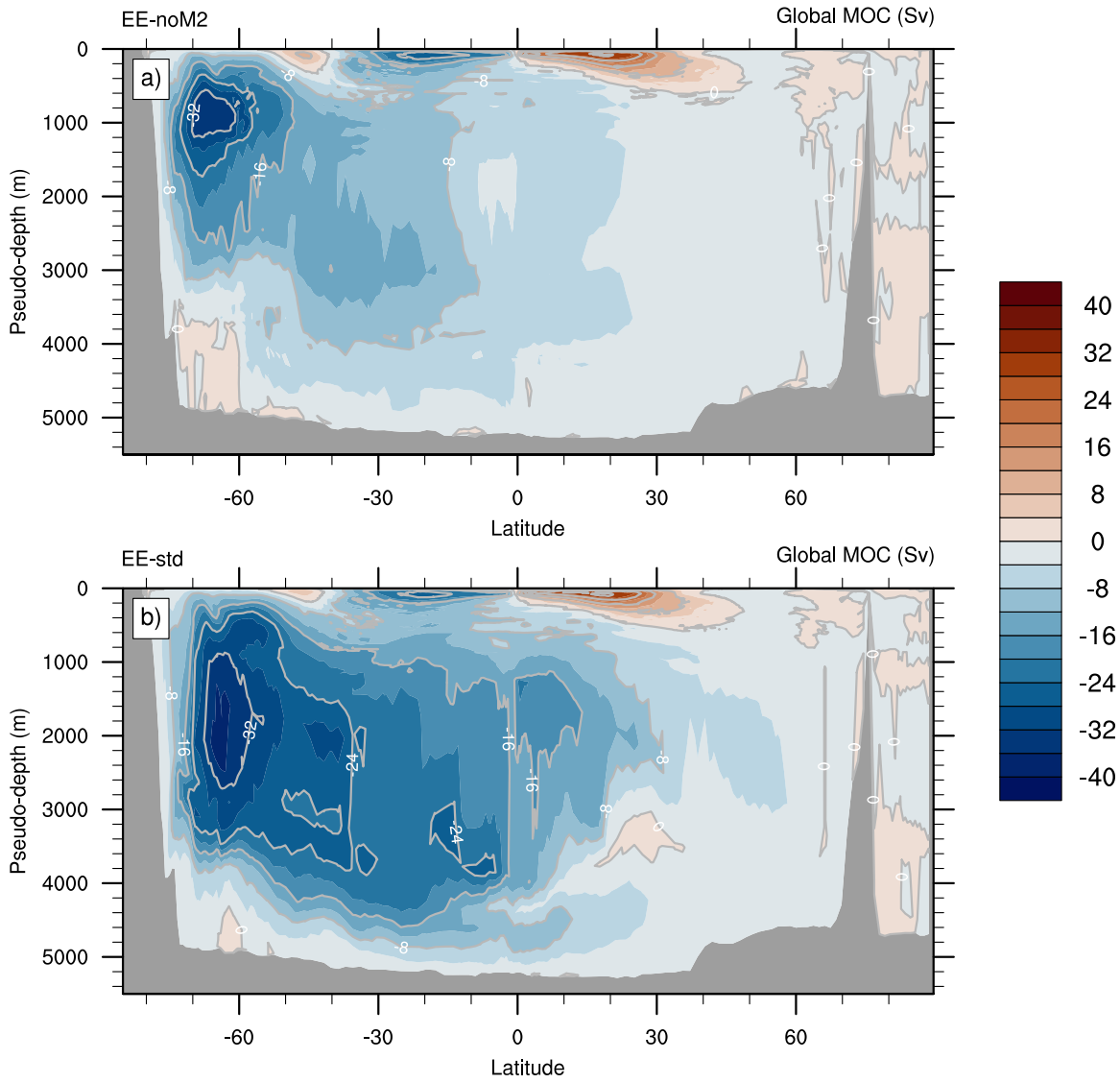

Figure 3. Global meridional overturning streamfunction (Sv) in EE-std (a) and EE-noM2 (b). Note that the MOC has been computed in density coordinates and reprojected to a pseudo-depth, following de Lavergne et al. (2017).

749

750

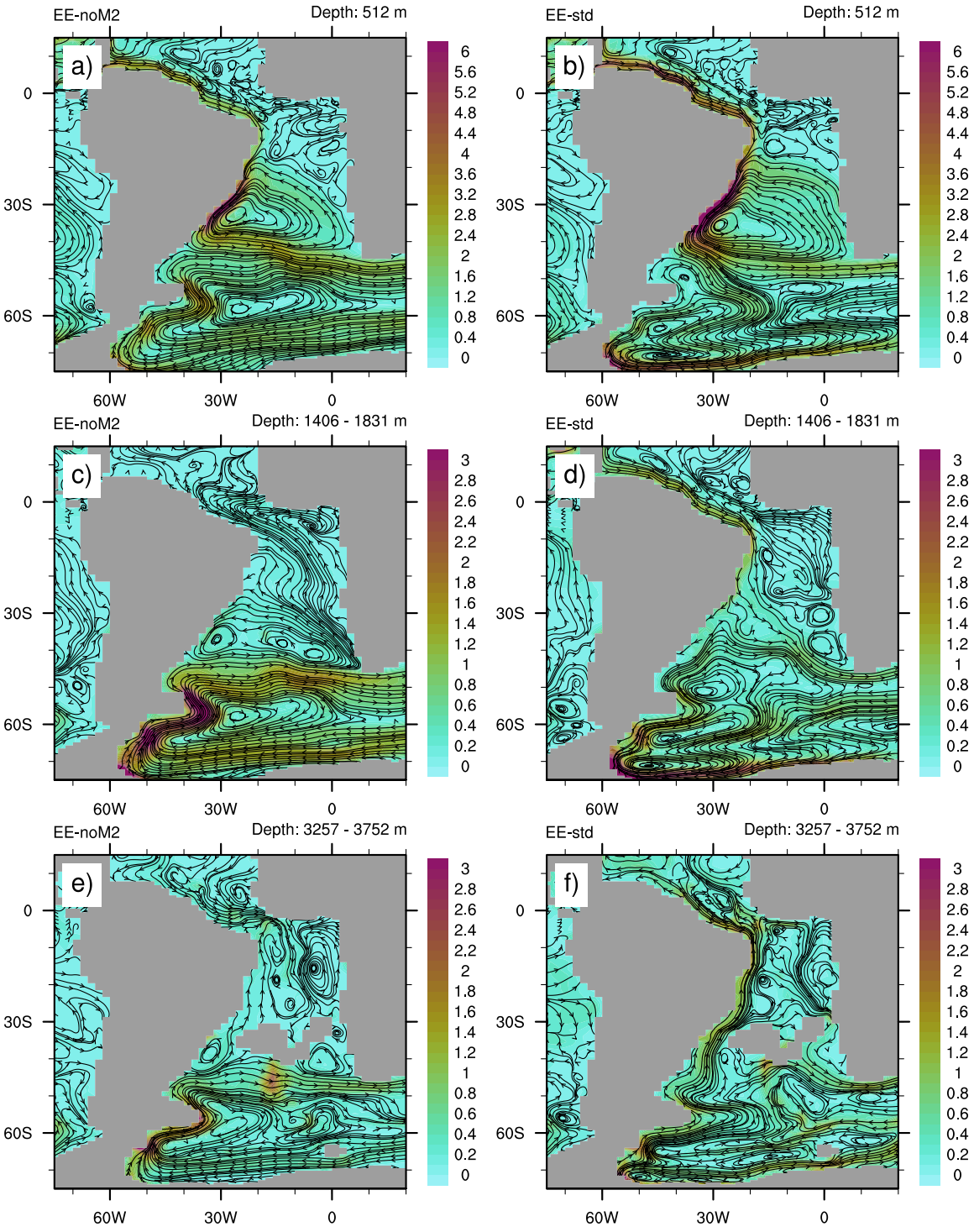

Figure 4. Ocean velocity (cm s^{-1}) at 500 m depth (a,b), averaged between 1400 and 1800 m (c, d) and averaged between 3250 and 3750 m (e, f) in EE-noM2 (a, c, e) and EE-std (b, d, f).

751

752

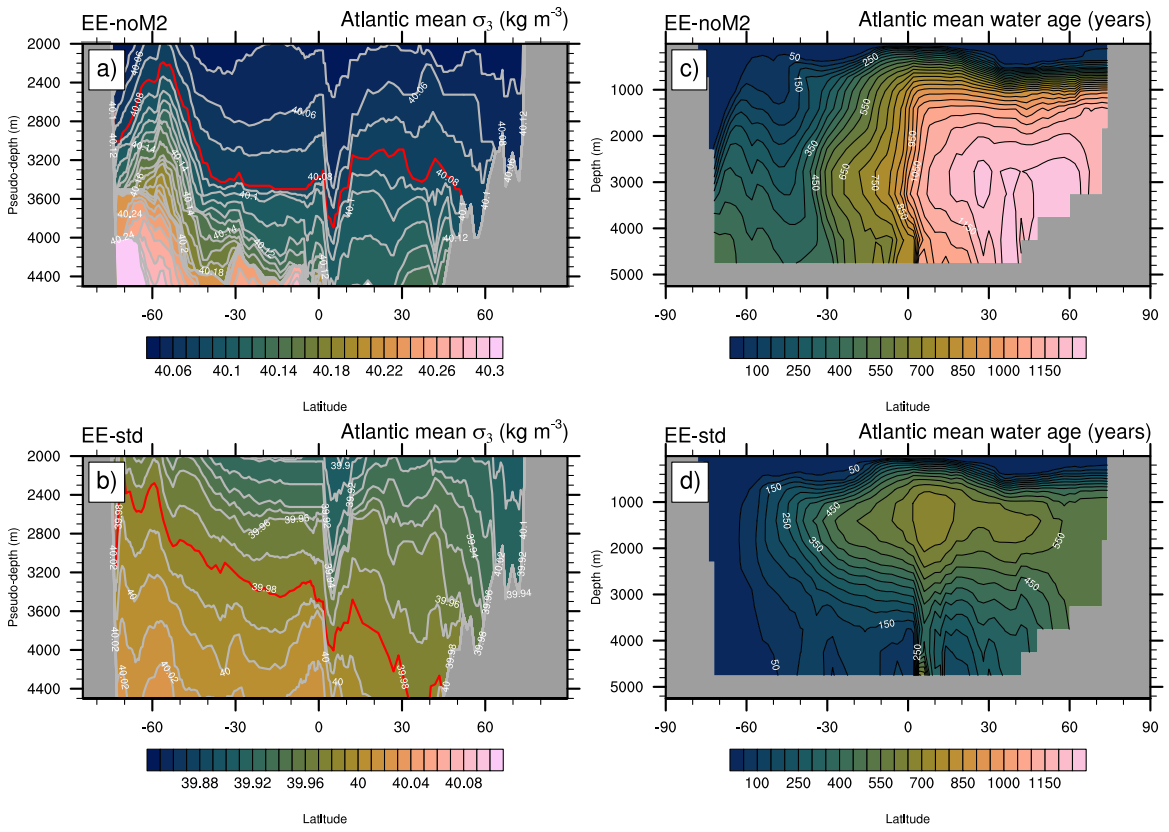

Figure 5. Zonally-averaged s_3 isopycnal profiles (kg m^{-3}) across the deep Atlantic in EE-noM2 (a) and EE-std (b) computed in density coordinates and reprojected to a pseudo-depth. The 40.08 and 39.98 kg m^{-3} s_3 contours are highlighted in red in (a) and (b) respectively, for easier visualization. Zonally averaged water age profile across the Atlantic in EE-noM2 (c) and EE-std (d). Note the different vertical axes between the two columns.

753

754

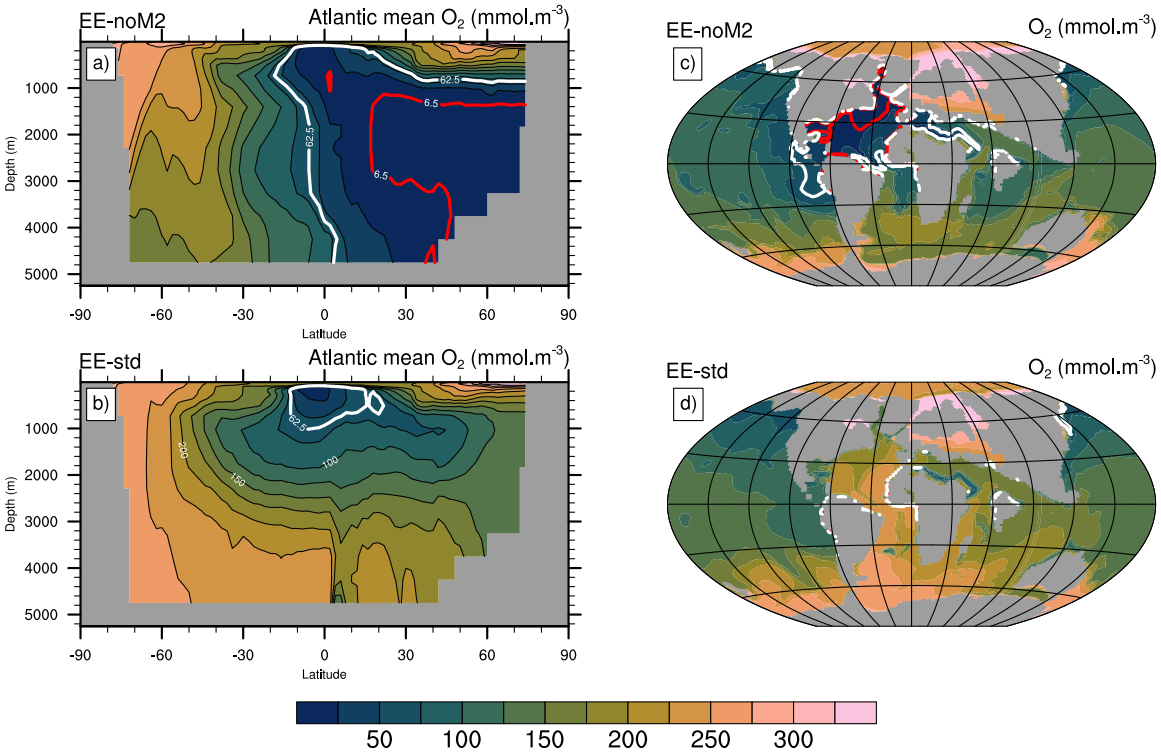

Figure 6. Zonally-averaged dissolved oxygen concentrations (mmol m^{-3}) across the Atlantic in EE-noM2 (a) and EE-std (b). Dissolved oxygen concentrations (mmol m^{-3}) at the seafloor in EE-noM2 (c) and EE-std (d). The hypoxic (62.5 mmol m^{-3}) and anoxic (6.5 mmol m^{-3}) thresholds (Laugié et al., 2021) are contoured in white and red, respectively.

755

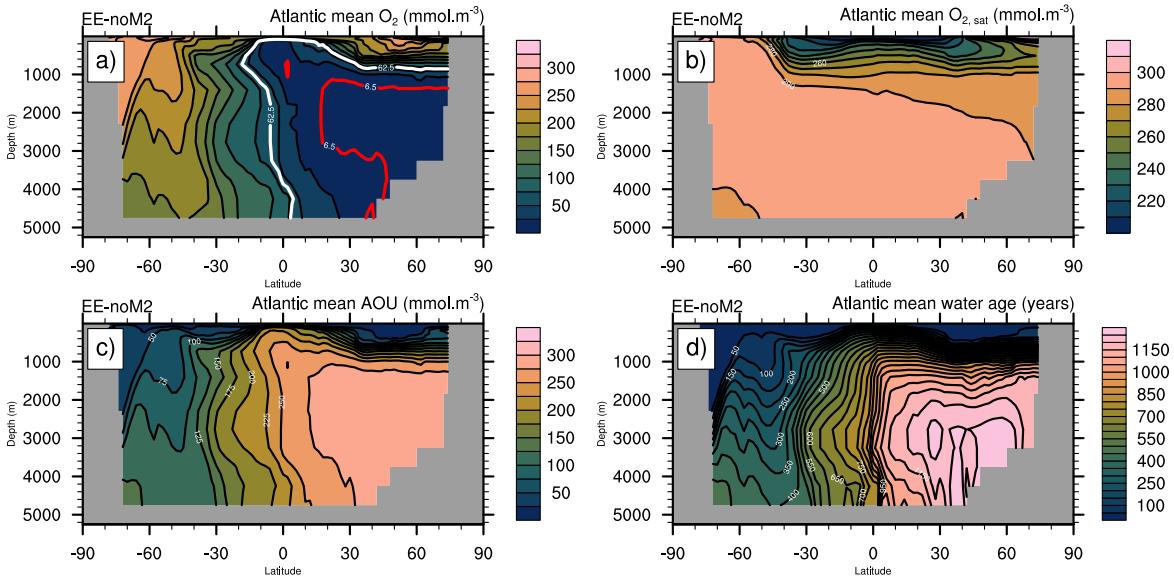

Figure 7. Zonally averaged (a) dissolved oxygen concentrations (mmol m^{-3}), (b) O_{2sat} (mmol m^{-3}), (c) AOU (mmol m^{-3}) and (d) water age (years) across the Atlantic in EE-noM2. Note the different scale in panel (b) relative to (a) and (c).

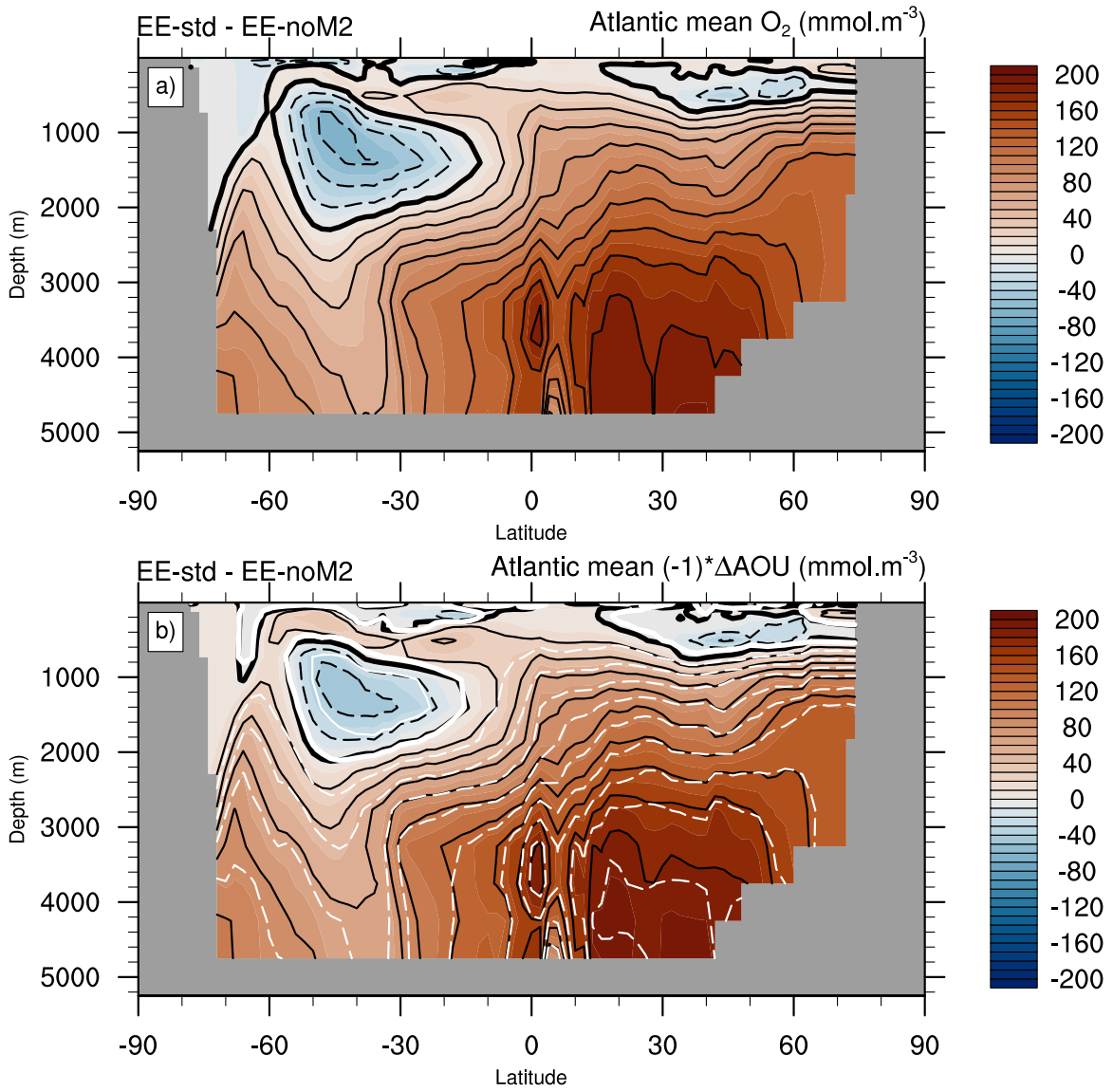

Figure 8. Zonally averaged (a) dissolved oxygen concentration difference (mmol m^{-3}) and (b) AOU difference (mmol m^{-3}) across the Atlantic between EE-std and EE-noM2 (shading and black contours). White contours denote the difference in water age between EE-std and EE-noM2 (positive solid and negative dashed).

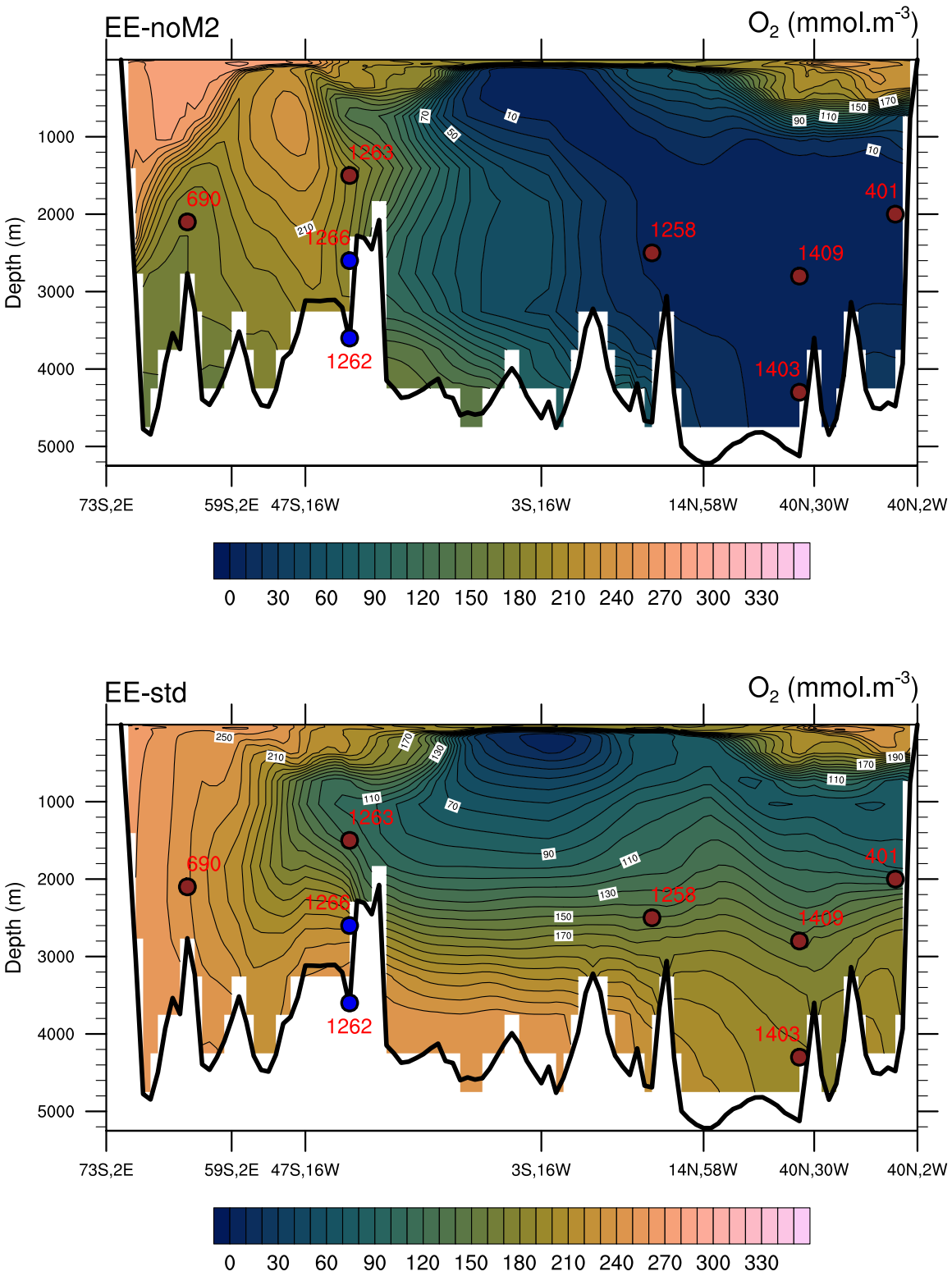

Figure 9. Dissolved oxygen concentration (mmol m^{-3}) transect across the Atlantic for EE-noM2 (a) and EE-std (b). The transect followed is shown on Fig. S3. At the exception of Sites 1262 and 1266 (blue color), for which oxygen-rich conditions have been reported, other Atlantic sites (brownish color) exhibit low oxygen conditions, according to proxy data.

760

References

Aumont, O., Ethé, C., Tagliabue, A., Bopp, L., Gehlen, M., 2015. PISCES-v2: an ocean biogeochemical model for carbon and ecosystem studies. Geosci. Model Dev. 8, 2465–2513. https://doi.org/10.5194/gmd-8-2465-2015

Blanke, B., Delecluse, P., 1993. Variability of the tropical Atlantic Ocean simulated by a general circulation model with two different mixed-layer physics. J. Phys. Oceanogr. 23, 1363–1388. https://doi.org/10.1175/1520-0485(1993)023<1363:VOTTAO>2.0.CO;2

Bopp, L., Resplandy, L., Untersee, A., Le Mezo, P., Kageyama, M., 2017. Ocean (de) oxygenation from the Last Glacial Maximum to the twenty-first century: insights from Earth System models. Philos. Trans. R. Soc. Math. Phys. Eng. Sci. 375, 20160323.

Bryan, K., Lewis, L.J., 1979. A water mass model of the World Ocean. J. Geophys. Res. Oceans 84, 2503–2517. https://doi.org/10.1029/JC084iC05p02503

Carmichael, M.J., Inglis, G.N., Badger, M.P.S., Naafs, B.D.A., Behrooz, L., Remmelzwaal, S., Monteiro, F.M., Rohrssen, M., Farnsworth, A., Buss, H.L., Dickson, A.J., Valdes, P.J., Lunt, D.J., Pancost, R.D., 2017. Hydrological and associated biogeochemical consequences of rapid global warming during the Paleocene-Eocene Thermal Maximum. Glob. Planet. Change 157, 114–138. https://doi.org/10.1016/j.gloplacha.2017.07.014

Cimoli, L., Mashayek, A., Johnson, H.L., Marshall, D.P., Naveira Garabato, A.C., Whalen, C.B., Vic, C., De Lavergne, C., Alford, M.H., MacKinnon, J.A., Talley, L.D., 2023. Significance of Diapycnal Mixing Within the Atlantic Meridional Overturning Circulation. AGU Adv. 4, e2022AV000800. https://doi.org/10.1029/2022AV000800

Clarkson, M.O., Lenton, T.M., Andersen, M.B., Bagard, M.-L., Dickson, A.J., Vance, D., 2021. Upper limits on the extent of seafloor anoxia during the PETM from uranium isotopes. Nat. Commun. 12, 399. https://doi.org/10.1038/s41467-020-20486-5

Crameri, F., Shephard, G.E., Heron, P.J., 2020. The misuse of colour in science communication. Nat. Commun. 11, 5444. https://doi.org/10.1038/s41467-020-19160-7

de Lavergne, C., Groeskamp, S., Zika, J., Johnson, H.L., 2022. The role of mixing in the large-scale ocean circulation, in: Ocean Mixing. Elsevier, pp. 35–63. https://doi.org/10.1016/B978-0-12-821512-8.00010-4

de Lavergne, C., Madec, G., Roquet, F., Holmes, R.M., McDougall, T.J., 2017. Abyssal ocean overturning shaped by seafloor distribution. Nature 551, 181–186. https://doi.org/10.1038/nature24472

de Lavergne, C., Vic, C., Madec, G., Roquet, F., Waterhouse, A.F., Whalen, C.B., Cuypers, Y., Bouruet-Aubertot, P., Ferron, B., Hibiya, T., 2020. A Parameterization of Local and Remote Tidal Mixing. J. Adv. Model. Earth Syst. 12, e2020MS002065. https://doi.org/10.1029/2020MS002065

Dickson, A.J., Cohen, A.S., Coe, A.L., 2012. Seawater oxygenation during the Paleocene-Eocene Thermal Maximum. Geology 40, 639–642. https://doi.org/10.1130/G32977.1

Dickson, A.J., Rees-Owen, R.L., März, C., Coe, A.L., Cohen, A.S., Pancost, R.D., Taylor, K., Shcherbinina, E., 2014. The spread of marine anoxia on the northern Tethys margin during the Paleocene-Eocene Thermal Maximum: Tethys redox during the PETM. Paleoceanography 29, 471–488. https://doi.org/10.1002/2014PA002629

Dunne, J.P., Sarmiento, J.L., Gnanadesikan, A., 2007. A synthesis of global particle export from the surface ocean and cycling through the ocean interior and on the seafloor. Glob. Biogeochem. Cycles 21, 2006GB002907. https://doi.org/10.1029/2006GB002907

Egbert, G.D., Ray, R.D., 2000. Significant dissipation of tidal energy in the deep ocean inferred from satellite altimeter data. Nature 405, 775–778.
Evans, D., Sagoo, N., Renema, W., Cotton, L.J., Müller, W., Todd, J.A., Saraswati, P.K., Stassen, P., Ziegler, M., Pearson, P.N., Valdes, P.J., Affek, H.P., 2018. Eocene greenhouse climate revealed by coupled clumped isotope-Mg/Ca thermometry. Proc. Natl. Acad. Sci. 115, 1174–1179. https://doi.org/10.1073/pnas.1714744115
Fichefet, T., Maqueda, M.A.M., 1997. Sensitivity of a global sea ice model to the treatment of ice thermodynamics and dynamics. J. Geophys. Res. Oceans 102, 12609–12646. https://doi.org/10.1029/97JC00480
Gargett, A.E., 1984. Vertical eddy diffusivity in the ocean interior. J. Mar. Res. 42, 359–393. https://doi.org/10.1357/002224084788502756
Garrett, C., Kunze, E., 2007. Internal Tide Generation in the Deep Ocean. Annu. Rev. Fluid Mech. 39, 57–87. https://doi.org/10.1146/annurev.fluid.39.050905.110227
Gaspar, P., Grégoris, Y., Lefevre, J., 1990. A simple eddy kinetic energy model for simulations of the oceanic vertical mixing: Tests at station Papa and long-term upper ocean study site. J. Geophys. Res. Oceans 95, 16179–16193. https://doi.org/10.1029/JC095iC09p16179
Green, J.A.M., Huber, M., 2013. Tidal dissipation in the early Eocene and implications for ocean mixing. Geophys. Res. Lett. 40, 2707–2713. https://doi.org/10.1002/grl.50510
Green, M., Hadley-Pryce, D., Scotese, C., 2023. Phanerozoic (541 Ma-present day), in: A Journey Through Tides. Elsevier, pp. 157–184.
Heinemann, M., Jungclaus, J.H., Marotzke, J., 2009. Warm Paleocene/Eocene climate as simulated in ECHAM5/MPI-OM. Clim Past 5, 785–802. https://doi.org/10.5194/cp-5-785-2009
Heinze, M., Ilyina, T., 2015. Ocean biogeochemistry in the warm climate of the late Paleocene. Clim. Past 11, 63–79. https://doi.org/10.5194/cp-11-63-2015
Herold, N., Buzan, J., Seton, M., Goldner, A., Green, J.A.M., Müller, R.D., Markwick, P., Huber, M., 2014. A suite of early Eocene (~ 55 Ma) climate model boundary conditions. Geosci. Model Dev. 7, 2077–2090. https://doi.org/10.5194/gmd-7-2077-2014
Holmes, R.M., Zika, J.D., Griffies, S.M., Hogg, A.McC., Kiss, A.E., England, M.H., 2021. The Geography of Numerical Mixing in a Suite of Global Ocean Models. J. Adv. Model. Earth Syst. 13, e2020MS002333. https://doi.org/10.1029/2020MS002333
Hourdin, F., Foujols, M.-A., Codron, F., Guemas, V., Dufresne, J.-L., Bony, S., Denvil, S., Guez, L., Lott, F., Ghattas, J., Braconnot, P., Marti, O., Meurdesoif, Y., Bopp, L., 2013. Impact of the LMDZ atmospheric grid configuration on the climate and sensitivity of the IPSL-CM5A coupled model. Clim. Dyn. 40, 2167–2192. https://doi.org/10.1007/s00382-012-1411-3
Huber, M., Caballero, R., 2011. The early Eocene equable climate problem revisited. Clim. Past 7, 603–633. https://doi.org/10.5194/cp-7-603-2011
Hutchinson, D.K., De Boer, A.M., Coxall, H.K., Caballero, R., Nilsson, J., Baatsen, M., 2018. Climate sensitivity and meridional overturning circulation in the late Eocene using GFDL CM2.1. Clim. Past 14, 789–810. https://doi.org/10.5194/cp-14-789-2018
Ilyina, T., Heinze, M., 2019. Carbonate Dissolution Enhanced by Ocean Stagnation and Respiration at the Onset of the Paleocene-Eocene Thermal Maximum. Geophys. Res. Lett. 46, 842–852. https://doi.org/10.1029/2018GL080761
Jayne, S.R., 2009. The Impact of Abyssal Mixing Parameterizations in an Ocean General Circulation Model. J. Phys. Oceanogr. 39, 1756–1775. https://doi.org/10.1175/2009JPO4085.1
Krinner, G., Viovy, N., De Noblet-Ducoudré, N., Ogée, J., Polcher, J., Friedlingstein, P., Ciais, P., Sitch, S., Prentice, I.C., 2005. A dynamic global vegetation model for studies of the

coupled atmosphere-biosphere system. Glob. Biogeochem. Cycles 19, 2003GB002199. https://doi.org/10.1029/2003GB002199
Laugié, M., Donnadieu, Y., Ladant, J., Bopp, L., Ethé, C., Raisson, F., 2021. Exploring the Impact of Cenomanian Paleogeography and Marine Gateways on Oceanic Oxygen. Paleoceanogr. Paleoclimatology 36, e2020PA004202. https://doi.org/10.1029/2020PA004202
Lazar, A., Madec, G., Delecluse, P., 1999. The Deep Interior Downwelling, the Veronis Effect, and Mesoscale Tracer Transport Parameterizations in an OGCM. J. Phys. Oceanogr. 29, 2945–2961. https://doi.org/10.1175/1520-0485(1999)029<2945:TDIDTV>2.0.CO;2
Liu, Z., Pagani, M., Zinniker, D., DeConto, R., Huber, M., Brinkhuis, H., Shah, S.R., Leckie, R.M., Pearson, A., 2009. Global cooling during the Eocene-Oligocene Climate Transition. Science 323, 1187–1190.
Lu, W., Rickaby, R.E.M., Hoogakker, B.A.A., Rathburn, A.E., Burkett, A.M., Dickson, A.J., Martínez-Méndez, G., Hillenbrand, C.-D., Zhou, X., Thomas, E., Lu, Z., 2020. I/Ca in epifaunal benthic foraminifera: A semi-quantitative proxy for bottom water oxygen in a multi-proxy compilation for glacial ocean deoxygenation. Earth Planet. Sci. Lett. 533, 116055. https://doi.org/10.1016/j.epsl.2019.116055
Lunt, D.J., Bragg, F., Chan, W.-L., Hutchinson, D.K., Ladant, J.-B., Morozova, P., Niezgodzki, I., Steinig, S., Zhang, Z., Zhu, J., Abe-Ouchi, A., Anagnostou, E., De Boer, A.M., Coxall, H.K., Donnadieu, Y., Foster, G., Inglis, G.N., Knorr, G., Langebroek, P.M., Lear, C.H., Lohmann, G., Poulsen, C.J., Sepulchre, P., Tierney, J.E., Valdes, P.J., Volodin, E.M., Dunkley Jones, T., Hollis, C.J., Huber, M., Otto-Bliesner, B.L., 2021. DeepMIP: model intercomparison of early Eocene climatic optimum (EECO) large-scale climate features and comparison with proxy data. Clim. Past 17, 203–227. https://doi.org/10.5194/cp-17-203-2021
Lunt, D.J., Huber, M., Anagnostou, E., Baatsen, M.L.J., Caballero, R., DeConto, R., Dijkstra, H.A., Donnadieu, Y., Evans, D., Feng, R., Foster, G.L., Gasson, E., Von Der Heydt, A.S., Hollis, C.J., Inglis, G.N., Jones, S.M., Kiehl, J., Kirtland Turner, S., Korty, R.L., Kozdon, R., Krishnan, S., Ladant, J.-B., Langebroek, P., Lear, C.H., LeGrande, A.N., Littler, K., Markwick, P., Otto-Bliesner, B., Pearson, P., Poulsen, C.J., Salzmann, U., Shields, C., Snell, K., Stärz, M., Super, J., Tabor, C., Tierney, J.E., Tourte, G.J.L., Tripati, A., Upchurch, G.R., Wade, B.S., Wing, S.L., Winguth, A.M.E., Wright, N.M., Zachos, J.C., Zeebe, R.E., 2017. The DeepMIP contribution to PMIP4: experimental design for model simulations of the EECO, PETM, and pre-PETM (version 1.0). Geosci. Model Dev. 10, 889–901. https://doi.org/10.5194/gmd-10-889-2017
MacKinnon, J.A., Zhao, Z., Whalen, C.B., Waterhouse, A.F., Trossman, D.S., Sun, O.M., St. Laurent, L.C., Simmons, H.L., Polzin, K., Pinkel, R., Pickering, A., Norton, N.J., Nash, J.D., Musgrave, R., Merchant, L.M., Melet, A.V., Mater, B., Legg, S., Large, W.G., Kunze, E., Klymak, J.M., Jochum, M., Jayne, S.R., Hallberg, R.W., Griffies, S.M., Diggs, S., Danabasoglu, G., Chassignet, E.P., Buijsman, M.C., Bryan, F.O., Briegleb, B.P., Barna, A., Arbic, B.K., Ansong, J.K., Alford, M.H., 2017. Climate Process Team on Internal Wave–Driven Ocean Mixing. Bull. Am. Meteorol. Soc. 98, 2429–2454. https://doi.org/10.1175/BAMS-D-16-0030.1
Madec, G., Imbard, M., 1996. A global ocean mesh to overcome the North Pole singularity. Clim. Dyn. 12, 381–388.
Madec, G., the NEMO team, 2016. NEMO ocean engine. Notes Pô Modélisation Inst. Pierre-Simon Laplace 27, ISSN No 1288-1619.
Marshall, J., Speer, K., 2012. Closure of the meridional overturning circulation through Southern Ocean upwelling. Nat. Geosci. 5, 171–180. https://doi.org/10.1038/ngeo1391
Meissner, K.J., Bralower, T.J., Alexander, K., Jones, T.D., Sijp, W., Ward, M., 2014. The Paleocene-Eocene Thermal Maximum: How much carbon is enough? Paleoceanography 29, 946–963. https://doi.org/10.1002/2014PA002650

Melet, A., Legg, S., Hallberg, R., 2016. Climatic Impacts of Parameterized Local and Remote Tidal Mixing. J. Clim. 29, 3473–3500. https://doi.org/10.1175/JCLI-D-15-0153.1
Melet, A.V., Hallberg, R., Marshall, D.P., 2022. The role of ocean mixing in the climate system, in: Ocean Mixing. Elsevier, pp. 5–34. https://doi.org/10.1016/B978-0-12-821512-8.00009-8
Merryfield, W.J., Holloway, G., Gargett, A.E., 1999. A Global Ocean Model with Double-Diffusive Mixing. J. Phys. Oceanogr. 29, 1124–1142. https://doi.org/10.1175/1520-0485(1999)029<1124:AGOMWD>2.0.CO;2
Meurdesoif, Y., Caubel, A., Lacroix, R., Dérouillat, J., Nguyen, M.H., 2016. XIOS tutorial. Httpforgeipsljussieufrioserverraw- Attach.-Tutorialpdf.
Middelburg, J.J., Soetaert, K., Herman, P.M.J., Heip, C.H.R., 1996. Denitrification in marine sediments: A model study. Glob. Biogeochem. Cycles 10, 661–673. https://doi.org/10.1029/96GB02562
Munk, W., Wunsch, C., 1998. Abyssal recipes II: Energetics of tidal and wind mixing. Deep Sea Res. 45, 1977–2010.
Munk, W.H., 1966. Abyssal recipes. Deep Sea Res. 13, 707–730.
Pälike, C., Delaney, M.L., Zachos, J.C., 2014. Deep-sea redox across the Paleocene-Eocene thermal maximum. Geochem. Geophys. Geosystems 15, 1038–1053. https://doi.org/10.1002/2013GC005074
Saenko, O.A., 2006. The Effect of Localized Mixing on the Ocean Circulation and Time-Dependent Climate Change. J. Phys. Oceanogr. 36, 140–160. https://doi.org/10.1175/JPO2839.1
Saenko, O.A., Merryfield, W.J., 2005. On the Effect of Topographically Enhanced Mixing on the Global Ocean Circulation. J. Phys. Oceanogr. 35, 826–834. https://doi.org/10.1175/JPO2722.1
Schmittner, A., Egbert, G.D., 2014. An improved parameterization of tidal mixing for ocean models. Geosci. Model Dev. 7, 211–224. https://doi.org/10.5194/gmd-7-211-2014
Schmittner, A., Green, J.A.M., Wilmes, S. -B., 2015. Glacial ocean overturning intensified by tidal mixing in a global circulation model. Geophys. Res. Lett. 42, 4014–4022. https://doi.org/10.1002/2015GL063561
Sepulchre, P., Caubel, A., Ladant, J.-B., Bopp, L., Boucher, O., Braconnot, P., Brockmann, P., Cozic, A., Donnadieu, Y., Dufresne, J.-L., Estella-Perez, V., Ethé, C., Fluteau, F., Foujols, M.-A., Gastineau, G., Ghattas, J., Hauglustaine, D., Hourdin, F., Kageyama, M., Khodri, M., Marti, O., Meurdesoif, Y., Mignot, J., Sarr, A.-C., Servonnat, J., Swingedouw, D., Szopa, S., Tardif, D., 2020. IPSL-CM5A2 – an Earth system model designed for multi-millennial climate simulations. Geosci. Model Dev. 13, 3011–3053. https://doi.org/10.5194/gmd-13-3011-2020
Sharoni, S., Halevy, I., 2023. Rates of seafloor and continental weathering govern Phanerozoic marine phosphate levels. Nat. Geosci. 16, 75–81. https://doi.org/10.1038/s41561-022-01075-1
Simmons, H.L., Jayne, S.R., Laurent, L.C.St., Weaver, A.J., 2004. Tidally driven mixing in a numerical model of the ocean general circulation. Ocean Model. 6, 245–263. https://doi.org/10.1016/S1463-5003(03)00011-8
Song, P., Sidorenko, D., Scholz, P., Thomas, M., Lohmann, G., 2023. The tidal effects in the Finite-volumE Sea ice–Ocean Model (FESOM2.1): a comparison between parameterised tidal mixing and explicit tidal forcing. Geosci. Model Dev. 16, 383–405. https://doi.org/10.5194/gmd-16-383-2023
St. Laurent, L., Garrett, C., 2002. The Role of Internal Tides in Mixing the Deep Ocean. J. Phys. Oceanogr. 32, 2882–2899. https://doi.org/10.1175/1520-0485(2002)032<2882:TROITI>2.0.CO;2

959 Talley, L., 2013. Closure of the Global Overturning Circulation Through the Indian, Pacific,
960 and Southern Oceans: Schematics and Transports. Oceanography 26, 80–97.
961 https://doi.org/10.5670/oceanog.2013.07
962 Thomas, D.J., Korty, R., Huber, M., Schubert, J.A., Haines, B., 2014. Nd isotopic structure of
963 the Pacific Ocean 70–30 Ma and numerical evidence for vigorous ocean circulation and ocean
964 heat transport in a greenhouse world. Paleoceanography 29, 454–469.
965 https://doi.org/10.1002/2013PA002535
966 Toggweiler, J.R., Samuels, B., 1998. On the Ocean's Large-Scale Circulation near the Limit
967 of No Vertical Mixing. J. Phys. Oceanogr. 28, 1832–1852. https://doi.org/10.1175/1520-
968 0485(1998)028<1832:OTOSLS>2.0.CO;2
969 Toggweiler, J.R., Samuels, B., 1995. Effect of drake passage on the global thermohaline
970 circulation. Deep Sea Res. Part Oceanogr. Res. Pap. 42, 477–500.
971 https://doi.org/10.1016/0967-0637(95)00012-U
972 Valcke, S., 2013. The OASIS3 coupler: a European climate modelling community software.
973 Geosci. Model Dev. 6, 373–388. https://doi.org/10.5194/gmd-6-373-2013
974 Vic, C., Naveira Garabato, A.C., Green, J.A.M., Waterhouse, A.F., Zhao, Z., Melet, A., De
975 Lavergne, C., Buijsman, M.C., Stephenson, G.R., 2019. Deep-ocean mixing driven by small-
976 scale internal tides. Nat. Commun. 10, 2099. https://doi.org/10.1038/s41467-019-10149-5
977 Wanninkhof, R., 1992. Relationship between wind speed and gas exchange over the ocean. J.
978 Geophys. Res. Oceans 97, 7373–7382. https://doi.org/10.1029/92JC00188
979 Weber, T., Thomas, M., 2017. Influence of ocean tides on the general ocean circulation in the
980 early Eocene. Paleoceanography 32, 553–570. https://doi.org/10.1002/2016PA002997
981 Whalen, C.B., de Lavergne, C., Naveira Garabato, A.C., Klymak, J.M., MacKinnon, J.A.,
982 Sheen, K.L., 2020. Internal wave-driven mixing: governing processes and consequences for
983 climate. Nat. Rev. Earth Environ. 1, 606–621. https://doi.org/10.1038/s43017-020-0097-z
984 Whitehead, J.A., 1998. Topographic control of oceanic flows in deep passages and straits.
985 Rev. Geophys. 36, 423–440. https://doi.org/10.1029/98RG01014
986 Wilmes, S.-B., Green, J.A.M., Schmittner, A., 2021. Enhanced vertical mixing in the glacial
987 ocean inferred from sedimentary carbon isotopes. Commun. Earth Environ. 2, 166.
988 https://doi.org/10.1038/s43247-021-00239-y
989 Winguth, A.M.E., Thomas, E., Winguth, C., 2012. Global decline in ocean ventilation,
990 oxygenation, and productivity during the Paleocene-Eocene Thermal Maximum: Implications
991 for the benthic extinction. Geology 40, 263–266. https://doi.org/10.1130/G32529.1
992 Xue, P., Chang, L., Dickens, G.R., Thomas, E., 2022. A Depth-Transect of Ocean
993 Deoxygenation During the Paleocene-Eocene Thermal Maximum: Magnetofossils in
994 Sediment Cores From the Southeast Atlantic. J. Geophys. Res. Solid Earth 127,
995 e2022JB024714. https://doi.org/10.1029/2022JB024714
996 Xue, P., Chang, L., Thomas, E., 2023. Abrupt Northwest Atlantic deep-sea oxygenation
997 decline preceded the Palaeocene-Eocene Thermal Maximum. Earth Planet. Sci. Lett. 618,
998 118304. https://doi.org/10.1016/j.epsl.2023.118304
999 Yao, W., Paytan, A., Wortmann, U.G., 2018. Large-scale ocean deoxygenation during the
1000 Paleocene-Eocene Thermal Maximum. Science 361, 804–806.
1001 https://doi.org/10.1126/science.aar8658
1002 Zhang, Y., De Boer, A.M., Lunt, D.J., Hutchinson, D.K., Ross, P., Van De Flierdt, T., Sexton,
1003 P., Coxall, H.K., Steinig, S., Ladant, J., Zhu, J., Donnadieu, Y., Zhang, Z., Chan, W., Abe-
1004 Ouchi, A., Niezgodzki, I., Lohmann, G., Knorr, G., Poulsen, C.J., Huber, M., 2022. Early
1005 Eocene Ocean Meridional Overturning Circulation: The Roles of Atmospheric Forcing and
1006 Strait Geometry. Paleoceanogr. Paleoclimatology 37, e2021PA004329.
1007 https://doi.org/10.1029/2021PA004329
1008 Zhang, Y., Huck, T., Lique, C., Donnadieu, Y., Ladant, J.-B., Rabineau, M., Aslanian, D.,

2020. Early Eocene vigorous ocean overturning and its contribution to a warm Southern Ocean. Clim. Past 16, 1263–1283. https://doi.org/10.5194/cp-16-1263-2020

Zhou, X., Thomas, E., Rickaby, R.E.M., Winguth, A.M.E., Lu, Z., 2014. I/Ca evidence for upper ocean deoxygenation during the PETM. Paleoceanography 29, 964–975. https://doi.org/10.1002/2014PA002702

Zhou, X., Thomas, E., Winguth, A.M.E., Ridgwell, A., Scher, H., Hoogakker, B.A.A., Rickaby, R.E.M., Lu, Z., 2016. Expanded oxygen minimum zones during the late Paleocene-early Eocene: Hints from multiproxy comparison and ocean modeling. Paleoceanography 31, 1532–1546. https://doi.org/10.1002/2016PA003020